Temperature-Controlled Nanoaperture Optical Trapping

by

Keiran Letwin
B.Sc., University of Ottawa, 2012
B.Eng., University of Victoria, 2022

A Dissertation Submitted in Partial Fulfillment of the
Requirements for the Degree of

MASTER OF APPLIED SCIENCE

in the Department of Electrical and Computer Engineering

We acknowledge and respect the Lək'^{w}əŋən (Songhees and X^{w}sepsəm/Esquimalt) Peoples on whose territory the university stands, and the Lək'^{w}əŋən and W̲SÁNEĆ Peoples whose historical relationships with the land continue to this day.

Temperature-Controlled Nanoaperture Optical Trapping

by

Keiran Letwin
B.Sc., University of Ottawa, 2012
B.Eng., University of Victoria, 2022

Supervisory Committee

Dr. R. Gordon, Supervisor
(Department of Electrical and Computer Engineering)

Dr. L. Smith, Departmental Member
(Department of Electrical and Computer Engineering)

Supervisory Committee

Dr. R. Gordon, Supervisor
(Department of Electrical and Computer Engineering)

Dr. L. Smith, Departmental Member
(Department of Electrical and Computer Engineering)

ABSTRACT

Nanoaperture optical trapping (NOT) enables the capture of single proteins to detect their conformational dynamics without labeling or tethering, thus preserving their structure. Protein folding is highly sensitive to environmental conditions, making the investigation of thermodynamic parameters a robust method for probing conformational stability. While previous studies have employed laser-induced heating to modulate the local temperature, such methods are limited in accessing broader temperature ranges. In this work, the low-temperature dynamics of individual Bovine Serum Albumin (BSA) are investigated using a custom-built temperature-controlled stage. The transitions between the normal (N) and fast (F) conformational states of BSA were uncovered. Notably, the N form exhibited a maximum occupancy at $21 \pm 1\,^{\circ}\mathrm{C}$, which was interpreted as the point of maximal thermodynamic stability for the compact N state relative to the F state. This approach enabled the extraction of single-molecule thermodynamic parameters without requiring modification to the protein's native structure, providing a multifaceted NOT method for broad applications.

Contents

List of Tables

List of Figures

ACKNOWLEDGEMENTS

I would like to thank:

My supervisor, Dr. Reuven Gordon, for providing this project and directing its fruition.

My friends and encounters who inspire my experiential reality; my tenacious family and dimensional brother, Matt; my mentors, colleagues, and students. Thank you for your continued support, conversations, and patience.

Gratitude, movement, and music.

DEDICATION

To meaning.

Chapter 1

Introduction

1.1 Motivation for Thesis

Protein conformational dynamics are fundamental to biological function. Enzymatic activity, ligand recognition, host-pathogen interactions, signal transduction, and structural organization rely on carefully orchestrated dynamics and environmental responsivity. Misfolded or conformationally unstable proteins are implicated in proteinopathies, including neurodegenerative diseases [2, 3] : Alzheimer's [2], Parkinson's [3], Huntington's [4]; prion-related disorders [5]; Type 2 diabetes [6]; systemic amyloidoses [7], and certain forms of cancer [8]. Although current ensemble-averaged techniques have elucidated many aspects of protein structure, they lack the ability to directly capture transient or heterogeneous conformational states at the single-molecule level and in real time.

This thesis presents a novel approach to studying protein conformational behavior using nanoaperture optical trapping (NOT). Specifically, double nanohole (DNH) optical tweezers are employed to capture individual proteins and monitor conformational transitions through changes in transmitted light intensity. This technique is a label-free approach with high sensitivity and detection with minimal photodamage due to the use of low optical powers thanks to plasmonic field enhancement at the nanoscale. Unlike previous studies, this experimental setup integrates precise thermal control, enabling a novel methodology to probe temperature-dependent conformational changes with necessary temporal resolution (10–100 µs scale). By combining NOT, thermal modulation, and signal analysis, this work demonstrates a platform for real-time analysis of protein stability and folding landscapes under

tunable environmental conditions.

1.1.1 Design and Development of Temperature-Controlled Nanoaperture Optical Trapping Experimental Set-up

During NOT experiments, where single-molecule sensitivity enables detection of subtle conformational transitions, the ability to modulate and stabilize sample temperature is essential for conducting thermodynamic analyses. However, integrating conventional active heating or cooling systems, such as those involving fans or fluid circulation, poses significant challenges due to mechanical vibrations, electromagnetic interference, and spatial constraints inherent to high-resolution optical systems. To maintain thermal stability without introducing noise or optical misalignment, a temperature-controlled stage must be designed and implemented. Its effectiveness; however, depends on the use of appropriate materials that preserve the sensitivity and alignment precision required for NOT experiments.

1.1.2 Conformational Dynamic Analysis of Proteins through Low-temperature Optical Trapping

Protein conformational stability is inherently governed by temperature-dependent thermodynamic forces [9]. Thermal energy mediates the equilibrium between folded and unfolded conformational states by altering the balance between enthalpic stabilization (hydrogen bonding, van der Waals forces) and entropic contributions (solvent and chain interactions) [9, 10]. At moderately low temperatures, reduced molecular motion and enthalpic contributions dominate, causing proteins to likely favour their ordered, N-state conformation. As temperature increases, thermal fluctuations disrupt the non-covalent interactions that maintain the tertiary structure, causing partial unfolding or denaturation.

The temperature-dependent equilibrium between the conformational states can be described by the Gibbs free energy change (ΔG), which reflects the balance of enthalpic and entropic contributions to folding [9, 10]. By examining how ΔG varies with temperature, often using the Gibbs-Helmholtz equation, quantification of protein stability and identification of critical transition points, such as melting temperature (T_m) or denaturation thresholds [11] is possible.

Low-temperature regimes are not as well characterized as their high-temperature

counterparts with regard to: cold denaturation, intermediate folding states, stability points, and the environmental sensitivity of folding mechanisms. The experimental separation of the enthalpic and entropic contributions to folding proves challenging, leaving room for other analytical attempts which utilize thermodynamic parameters to probe protein conformational behaviour.

1.2 Organization of Thesis

Chapter 2 provides the theoretical and experimental foundations for studying protein conformational dynamics using thermodynamic principles and NOT. Traditional methods are reviewed alongside the Gibb's free energy framework for analyzing folding behaviour. NOT is introduced as a label-free, single-molecule technique, which can resolve structural transitions of protein conformational states via laser transmission intensity fluctuations. Alluding to prior work with bovine serum albumin (BSA), this section aims to emphasize the importance of extending analysis to lower temperature regimes to better characterize native and intermediate states, highlighting NOT's broader implications for thermodynamic protein analysis.

Chapter 3 outlines methods used in the design and implementation of a temperature-controlled NOT set-up. Improvements made to a previous temperature-controlled stage design are provided, followed by detailed procedures for the nanofabrication of gold DNH samples and the preparation of BSA protein solutions. An adapted protocol for trapping single molecules at controlled temperatures is presented, which is based on the conventional NOT approach developed by Dr. Gordon's nanoplasmonics group.

Chapter 4 presents results obtained using a temperature-controlled NOT system. The first section outlines preliminary proof-of-concept experiments that demonstrate the efficacy of the setup for single-molecule thermodynamic studies. The next section details a study of conformational transitions in the model protein BSA at low temperatures, showcasing the system's capability to resolve temperature-dependent folding behaviour. In particular, the discovery of a low-temperature conformational stability point is identified through a novel analysis methodology based on Arrhenius' state transition theory.

Chapter 5 provides suggestions for future work, including modification to the gold DNH sample for improved thermal performance, as well as enhancements to the temperature-controlled NOT setup to improve experiment precision and flexibility.

Chapter 6 concludes this thesis.

1.2.1 Author's Contribution

The work presented in "Section 4.2" was published as part of The Journal of Physical Chemistry B special issue "Naomi Halas and Peter Nordlander Festschrift". © 2025 American Chemical Society.

Keiran Letwin, Matthew Peters, and Reuven Gordon. "Conformational Stability at Low Temperatures Using Single Protein Nanoaperture Optical Tweezers", *J. Phys. Chem. B*, 2025, **129**, 2402–2407. DOI: 10.1021/acs.jpcb.4c0787.

K.L. designed and built the temperature-controlled stage, devised and performed experiments, performed analysis, and assisted in writing the manuscript. The work was inspired by previous publication by M.P. ([1]). R.G. advised on the temperature-controlled stage design, experiments, analysis, and writing the manuscript. Not mentioned in the publication, is Dr. Mohsen Akbari, who provided insight on material selection for the stage design.

Chapter 2

Background

This chapter is structured hierarchically. It begins with a broad overview of methods for studying protein conformational states, and then narrows to a foundational, yet motivating discussion on the use of NOT in conjunction with thermodynamic parameters as an enhancement to these approaches.

2.1 The Study of the Conformational States of Proteins : Label and Label-Free Methods

Proteins are macromolecules with physiological functions that depend on their conformation- the three-dimensional adopted shape determined by their compositional, primary amino acid sequence and interactions with their immediate cellular milieu [12]. The conformation arises through a hierarchical organization of structural levels wherein the primary sequence folds into a secondary structure of α-helices and β-pleated sheets by hydrogen bonding, followed by tertiary packing by hydrophobic and ionic interactions, hydrogen bonds, and disulfide bridges. Multiple peptide chains may conglomerate to form quaternary structures [13]. A protein; however, does not remain in one conformational state. It is a Boltzmann ensemble of conformations [14]. It may have a dominant tertiary or quaternary conformation, but will access smaller fluctuating populations weighted by their free energies, in response to environmental cues. Fluctuations are described in terms of dynamic or static flexibility [14]. Dynamic flexibility refers to the rate of transition between conformations and pertains to energy maxima (or barriers between states) whereas static flexibility refers to the energy minima and equilibrium quantities of the states themselves [14]. The

precise orchestration of protein flexibility is required for maintaining physiological equilibrium, as cellular processes involve dynamic conformational states of proteins. In particular, intrinsically disordered proteins (IDPs) are an extreme of this dynamic spectrum [15]. They lack a fixed tertiary structure, yet retain functional versatility since they are conformationally fluid at equilibrium. They sample a wide ensemble of conformations to accommodate multiple binding partners, and are usually hubs in signaling pathways.

Consequently, structural changes that arise from protein misfolding can disrupt this balance and become pathogenic. Misfolding can arise from genetic mutations, environmental shifts, oxidative stress, or errors during post-translational modifications [16]. In addition to loss of function [17], misfolded proteins can self-aggregate into toxic amyloid fibrils and oligomers. For example, prions, which are proteinaceous pathogenic agents, have spatial properties that can induce conformational changes in normally folded, similar proteins, leading to amyloids in the brain [5].

Cells have corrective mechanisms to manage protein homeostasis: molecular chaperones assist in proper folding or target unstable proteins; the degradation of misfolded proteins by ubiquitin-proteasome systems [18]; and autophagy of larger aggregates [4]. However, disease progression may continue unabated, so efforts to mitigate protein misfolding disorders increasingly focus on molecular interventions. Developing therapies requires a precise understanding of the early conformational transitions that initiate misfolding. Designing agents that target these intermediate states is challenging because they must exhibit high specificity while minimizing toxicity. Consequently, gaining improved structural insights into folding pathways is critical to the development of more selective therapeutics, specifically those that perturb aggregation processes [19].

It is therefore vital that protein conformation dynamics and stability states are understood for medical applications and fundamental research. In particular, drug development largely depends on protein stability, from the point of discovery, production, storage and transportation, to pharmacokinetics. Each stage is subjectively indicative of environmental composition, such as buffer formulation, in research practices. The conformation's compactness and energetically-dependent folding behavior can therefore reveal optimal stability conditions such as pH, ionic strength, and temperature. By studying the influence of these parameters, optimization of a protein's use can be understood, or further, provide the ability to engineer proteins as novel therapeutic agents (for example, monoclonal antibodies) [20, 21, 22, 23].

2.1.1 Label-Based Methods

Current methods used to study protein stability are label-based or label-free. The most widely label-based method is Förster Resonance Energy Transfer (FRET), which quantifies the nanometer proximity between two fluorescently labeled macromolecules. Labeling involves the attachment of two fluorophores to a biomolecule or molecular complex. Although effective, labeling can be technically challenging and costly, and has the potential to interrupt the integrity of the protein under investigation [24, 25, 26]. As a result label-free methods have gained interest due to exemplary resolution, sensitivity, specificity, and the potential for high-throughput for a range of proteins without overt consideration for catered optimization [27, 28].

2.1.2 Label-Free Methods

Examples of label-free methods include: intrinsic fluorescence spectroscopy, UV absorbance spectroscopy, and light scattering. Intrinsic fluorescence spectroscopy relies on the natural emission of aromatic amino acids, particularly tryptophan, to monitor conformational changes during unfolding or denaturation. This approach can be sensitive and non-invasive but is limited to proteins that contain fluorescent residues and can be inadvertently influenced by environmental conditions such as pH or ionic strength [29]. UV absorbance spectroscopy tracks changes in UV absorbance ratios at characteristic wavelengths, which reflect protein concentration and conformation. Although it is rapid and easy to implement, this method has lower sensitivity and can be affected by the presence of buffer components or contaminants [30]. Light scattering techniques, including static and dynamic light scattering, are widely used to detect aggregation events that often accompany protein unfolding. Unfortunately, these methods often require careful calibration, can fail to distinguish between different types of aggregates, and do not always provide structural detail [31].

2.2 Thermodynamic Approaches for Label-Free Methods

Other label-free methods employ temperature as a strategy to resolve protein conformational dynamics and stability. During protein heating, differential scanning calorimetry (DSC) and differential scanning fluorimetry (DSF) detect changes in the

heat capacity and fluorescence. The latter is susceptible to producing false results due to unwanted interactions between fluorescent dyes and the protein, and some proteins may not produce significant fluorescent changes upon unfolding [32]. The former may produce detailed thermodynamic parameter data, such as enthalpy and entropy, but it requires relatively large amounts of purified protein and specialized equipment, limiting its throughput [33].

A protein's thermodynamic parameters are used as a proxy for its stability through the calculation of ΔG [9, 10]. It assumes a two-state isothermal-isobaric closed system where a protein reversibly transitions from its native (folded) to its unfolded conformation. Specifically, at its melting temperature, T_m, the protein is found to be equally folded and unfolded [34] and $\Delta G = 0$. If the equilibrium constant is known, the enthalpy (ΔH) and entropy (ΔS) of unfolding can be determined, since the following equation holds:

$$\Delta G = \Delta H - T\Delta S = -RT \ln K \tag{2.1}$$

where:

R is the universal gas constant,

T is the absolute temperature,

K is the equilibrium constant.

DSC and DSF utilize this relation [35, 36, 37, 38, 39], but this approach assumes a constant temperature, so is only valid at a specific point, and cannot discern the degree to which stability is enthalpy or entropy-related. Further, it cannot account for proteins that transition through intermediate or non-cooperative states.

An improved thermodynamic framework for assessing protein stability adopts a more general model than 2.1 termed the Gibbs-Helmholtz equation [11]. It includes van't Hoff enthalpy change (ΔH_{vH}) and heat capacity change (Δc_p) to account for temperature dependence. Δc_p, a parameter critical to proteins, enables continuous modeling of ΔG(T) beyond the assumption of a two-state folding/unfolding system, so protein stability can be examined at broader and more physiologically relevant temperatures other than T_m. The Gibbs-Helmholtz relation is expressed as:

$$\Delta G(T) = \Delta H_{vH}\left(1 - \frac{T}{T_m}\right) - \Delta c_p\left((T_m - T) + T\ln\frac{T}{T_m}\right) \tag{2.2}$$

For example, in the case of the well-characterized BSA, [40] used three complementary techniques: fluorescence spectroscopy (as a local site-specific probe), circular dichroism (as a global probe for α-helical structure) and differential scanning calorimetry (to probe the energetics of unfolding) and the Gibbs-Helmholtz equation with the values $T_m = 338.2\,\mathrm{K}$, $\Delta H_{vH} = 31\,\mathrm{kcal/mol}$, and $\Delta c_p = 1.0\,\mathrm{kcal/(K \cdot mol)}$ during state transitions, to find a maximum stability at approximately 36°C (where ΔG is highest). However, BSA undergoes significant structural changes above 30°C [41], so the validity of this approach may be limited, highlighting the need for untargeted stability analyses that characterize informational ensembles without assuming thermodynamic parameters in advance.

2.3 Using Thermodynamic Approaches with Nanoaperture Optical Trapping

Light-matter interaction was first described as the deflection of a comet's tail away from the sun by Kepler in 1619 [42]. The light provided a mechanical force, an idea that was expanded to the exertion of pressure due to momentum by Maxwell in the 19th century [43]. This radiation pressure was limited in that the forces involved were so miniscule that it necessarily be enacted in a vacuum- resulting in the only meaningful application being solar sail propulsion, albeit a theoretical novelty at that time [43]. It was not until the invention of the laser in the 1960s that highly focused coherent light beams could exert measurable, practical optical forces; and the insight of Dr. Arthur Ashkin that small particles only required small forces that optical trapping was possible. Ashkin demonstrated that micrometer-sized dielectric particles could be trapped or accelerated using two counterpropagating lasers because of the finite balance between an optical levitation force, the particle weight, and gravity [43] [42]. Then in 1986, single beam trapping of tobacco mosaic viruses and bacteria *Escherichia coli* was achieved, which eventually led to its interdisciplinary use, resulting in Ashkin's Nobel Prize in Physics in 2018 [44]. It was demonstrated that electromagnetic waves can be considered as a large collection of photons, each with a quantized amount of momentum that can be transferred to matter, providing the balancing forces required for trapping with few optical components. Improvements made to the initial trapping set-up have led to modern traps that are capable of a high degree of control over several trapping parameters such as trap strength and location.

High-resolution measurements of small trapped particle displacements (forces) are currently possible due to developments in other optics-related fields. For instance, the introduction of near-field optics has allowed work in the nanometer regime by overcoming the limitations imposed by the diffraction limit of free-space laser beams. In 2023, by employing an adjustable plasmonic optical nanogap, direct trapping of single molecules as small as $\sim$5 Å (0.57nm) in solution has been achieved [45].

The following section is an overview of the label-free method, NOT. The details of all relevant theory for this methodology will be provided followed by its specific use as a platform for the previously discussed thermodynamic approaches to studying protein conformation dynamics with BSA as a model system.

2.3.1 Optical Forces in the Rayleigh Regime

To represent the forces present in a particle-light system, an electromagnetic model is required. For particles made of linear, isotropic material with sizes much smaller than the wavelength of light, the Rayleigh regime applies ($r \ll \lambda$) [43, 42]. The particle can be modeled as a point electric dipole, which experiences Lorentz force in an electromagnetic field, and is written accordingly:

$$\langle \mathbf{F} \rangle = \frac{1}{4}\mathrm{Re}(\alpha_p)\nabla|\mathbf{E}|^2 + \sigma(\alpha_p)\frac{1}{2c}\mathrm{Re}\left(\mathbf{E}\times\mathbf{H}^*\right) + \sigma(\alpha_p)\frac{1}{c}\nabla\times\left(\epsilon_0\frac{1}{4\omega i}\mathbf{E}\times\mathbf{E}^*\right) \quad (2.3)$$

where:

$\langle \mathbf{F} \rangle$ is the time-averaged force acting on the particle,

α_p is the polarizability of the dielectric particle,

$\mathbf{E}$ and $\mathbf{H}$ are the electric and magnetic fields,

c is the speed of light,

$\sigma(\alpha_p)$ is the particle cross-section, assuming it is a sphere.

The first and second terms in 2.3 represent the gradient and scattering forces [42]. The third is the spin-curl force, which arises from the curl of the spin angular momentum of the incident beam. Since this work uses linearly polarized light, this term is omitted.

The polarizability determines all three force components and is expressed as:

$$\alpha_p = \frac{\alpha_0}{1 - i\frac{\alpha_0 k^3}{6\pi\epsilon_m}}$$

where:

$\alpha_0 = 4\pi\epsilon_0 n_m^2 r^3 \left(\frac{m^2-1}{m^2+2}\right)$ is the Clausius-Mossotti relation,

r is the particle radius,

$m = \frac{n_p}{n_m}$ is the relative refractive index of the particle to the surrounding medium.

The gradient and scattering forces can be rewritten as [42]:

$$\vec{F}_{\text{grad}} = -\frac{2\pi n_0 r^3}{c}\left(\frac{m^2-1}{m^2+2}\right)\nabla I(\vec{r}) \tag{2.4}$$

where:

$I(\vec{r})$ is the time-averaged optical intensity at position $\vec{r}$.

$$\vec{F}_{\text{scat}} = \frac{8\pi n_0 k^4 r^6}{3c}\left(\frac{m^2-1}{m^2+2}\right)^2 I(\vec{r})\hat{z} \tag{2.5}$$

where:

$k = \frac{2\pi}{\lambda}$ is the wave number,

$\hat{z}$ is the direction of beam propagation.

It can be seen that optimizing the trap by tuning the polarizability is possible, since the gradient trapping strength is directly related to the dielectric contrast between the particle and the medium. If $m < 1$, the force can reverse direction. Moreover, it arises from the interaction of the induced dipole with the spatial variation of the electric field, or the gradient of intensity, causing the particle to move toward regions of higher or lower intensity depending on the value of m. When $m > 1$, the particle is attracted to the area of highest intensity (where rays are highly focused), which in this work, is at the centre of the incident Gaussian beam.

When the light scatters off of the particle, the change in momentum flux (from the Poynting vector) results in a scattering force in the direction of light propagation [43].

There are two key implications from the scaling of the forces in 2.4 and 2.5 with particle volume: the gradient force must be large enough to counteract the scattering force for stable trapping; and that any sufficiently small, non-absorbing particle can be trapped three-dimensionally. In practice; however, particles experience random motion due to thermal fluctuations, manifested as stochastic Brownian motion, which can be estimated from the particle's interaction with the solvent through the drag coefficient [46]:

$$F_{\text{drag}} = 6\pi\,\nu\,r\,v \tag{2.6}$$

where:

F_{drag} is the force due to drag,

ν is the dynamic viscosity of the fluid,

r is the radius of the particle,

v is the particle velocity relative to the fluid.

The magnitude of the resulting Brownian force fluctuates randomly, and for stable trapping, the optical gradient force must exceed the typical thermal fluctuations. As particle size decreases, Brownian motion becomes increasingly significant, potentially resulting in trap escape. Mitigation may involve increasing: viscous drag through particle tethering, m, or laser intensity- all of which have practical limitations, particularly the last, which risks particle photodamage and denaturation. Therefore, laser light confinement must be increased.

2.3.2 Subwavelength Optics and Nanoapertures

Subwavelength optics concerns the interaction between electromagnetic waves and objects with features less than half the wavelength. The transmission through nanoapertures is a facet of this field, particularly in a fixed-dimensional metal film.

Beginning with Bethe's aperture theory (1944) [47], which concerns how a normal incident plane wave interacts with a circular aperture in a perfectly conducting, infinite thin screen. The field does not simply pass through, but the transmission is modeled as radiation from induced dipoles.

Considering the case of the electromagnetic field having parallel components to the thin film. Using the quasi-static approximation, when compared to the spatial dependence, the time dependence of Maxwell's equation is negligible. Since the aperture is much smaller than the wavelength, it can be approximated as a magnetic dipole with polarizability that is geometrically governed. In the case of a circular aperture, this is $\alpha_m = \frac{8r^3}{3}$. The magnetic polarizability then dictates that the transmitted power emitted by the magnetic dipole is:

$$P = \frac{2Z_0\pi^3}{3\lambda^4}\left(\alpha_m H_0\right)^2 \tag{2.7}$$

where:

Z_0 is the free-space impedance,

λ is the wavelength of light,

α_m is the magnetic polarizability,

H_0 is the magnetic field amplitude of the incident light.

If 2.7 is normalized to the circular area, the transmission is inversely proportional to the fourth power of the light wave-length In essence, there are dominant field components outside of the aperture due to the magnetic dipole parallel to the surface, which has a moment that is induced by discontinuity of surface currents and charges caused by the aperture. As a result, after normalizing the transmitted power to the aperture area πr^2, it becomes proportional to the fourth power of the aperture radius, and inversely proportional to the fourth power of the wavelength, resulting in suppression of light through the aperture:

$$T \propto \left(\frac{r}{\lambda}\right)^4$$

The light diminishes with aperture radius reduction. However, different polarizabilities arise from different shaped apertures, so optical transmission may differ between apertures of the same area.

If the incident field has perpendicular components, the aperture is modeled as an electric dipole with a similar diffracted power formulation.

Although foundational, Bethe's theory was contradicted by Ebbessen (1998) by demonstrating extraordinary optical transmission (EOT) [48]. Light transmission was

doubled through a silver film with periodic apertures through resonant coupling to surface plasmon modes on the metal surface. Additionally, Bethe's theory is limited to the microwave regime, where the metal acts as a perfect conductor, and so does not consider the real response of the metal such as in the case of visible-IR regime [49].

2.3.2.1 Surface Plasmons

Since metals are not perfect conductors at shorter incident EM wavelengths they can absorb light, have losses, and support surface plasmon (SPs) waves- the coherent oscillation of electrons at a metal-dielectric boundary. Such behaviour is modeled using the Drude model which gives the metal's frequency-dependent relative permittivity, $\varepsilon(\omega)$ using electron motion [49]. It predicts a negative real part at a frequency below plasma frequency, and at a dielectric-metal interface, if one material has a negative permittivity with a large magnitude in the real part, a surface plasmon wave can form. It propagates with wave vector $\beta > k_0$, (the wave vector of light in free-space). This can be shown by solving for Maxwell's equations at the boundary, and is given by the dispersion relation:

$$\beta = k_0 \sqrt{\frac{\varepsilon_d \varepsilon_m}{\varepsilon_d + \varepsilon_m}}$$

The resulting SP is bound to the metal surface because its exponential decay sequesters it to a length of hundreds of nanometers into the dielectric and tens of nanometers into the metal. In the case of an isolated metallic NA, SPs exist as a non-propagating mode called localized surface plasmon (LSP). The oscillation is spatially confined to the edges of NA, causing strong electric field enhancement, especially at sharp corners, cusps or narrow gaps (termed hotspots), which are orders of magnitude stronger than the incident light field, producing strong gradient forces [50]. It is therefore sensible that since advent of lithography techniques to produce arbitrarily shaped metallic NAs, their incorporation into NOT for the purpose of concentrating light to sub-diffraction-limited spot sizes by inducing SPs is a given. In the case of our group, DNH apertures are integrated into the NOT setup to enhance gradient forces during trapping (see Figure 3.3).

2.3.2.2 Self-Induced Back Action

The potential well of a trap may be deepened to overcome the Brownian motion (thermal fluctuations) through a proposed mechanism called self-induced back action (SIBA) [51]. It is a dynamic mechanism in which the trapped particle modifies the trapping potential as it moves relative to the NA. Transmission through the NA is sensitive to the surrounding dielectric environment, so the presence of a dielectric object with a higher refractive index than the surrounding medium increases the effective refractive index near the aperture. If the particle drifts away from the aperture, the transmitted photon momentum decreases, and by Newton's third law, this change generates a reaction force that pulls the particle back toward the trap center. This feedback-enhanced trapping mechanism enables stable confinement with optical intensities up to twenty times lower than those required in conventional optical trapping, exemplifying a further advantage to NA integration into NOT.

2.3.3 Investigating Thermodynamic Parameters of Proteins using NOT for Protein Stability Analysis

NOT can be used to study protein conformational dynamics through investigation of their thermodynamic parameters. In terms of incident laser power, localized heating within the nanoaperture has been reported to be one degree Kelvin per milliwatt [52, 53, 54, 55, 56], so laser power tuning can probe structural changes of trapped proteins [57, 1]. This was first exemplified using BSA as a model system, where a reversible two-state transition was observed as transmission fluctuations of the incident laser through the nanoaperture during power incrementation [58].

2.3.3.1 BSA as a Model Protein System

It should be further explained that BSA serves as a valuable model for studying protein conformational dynamics due to its well-defined domain structure, high solubility, and sensitivity to environmental conditions. It is a 66 kDa water-soluble monomeric protein, composed of 583 amino acid residues, with approximate dimensions of 80 $\times$ 80 $\times$ 40 Å, and a hydrodynamic radius of 3.4nm [58]. It is the most abundant protein in mammalian blood plasma, present at concentrations of 40–50 mg/mL, and plays critical roles in the transport and binding of hydrophobic molecules.

Structurally, BSA consists of three homologous domains (I, II, and III), each

subdivided into two subdomains (A and B), which offers some predictability of its folding behaviour due to internal symmetry. These domains are stabilized by 17 disulfide bridges formed between the thiol groups of strategically positioned cysteine residues, and a single free sulfhydryl group (Cys34) located in a hydrophobic pocket of domain I. This disulfide network is not only essential for the stability of the compact, fully folded normal (N) state, characterized by a high degree of α-helicity and tightly packed hydrophobic domains shielded from the aqueous environment, but also creates multiple unfolding hinge points that generates structural variability and heterogeneous conformational states [59, 60, 61, 62, 63].

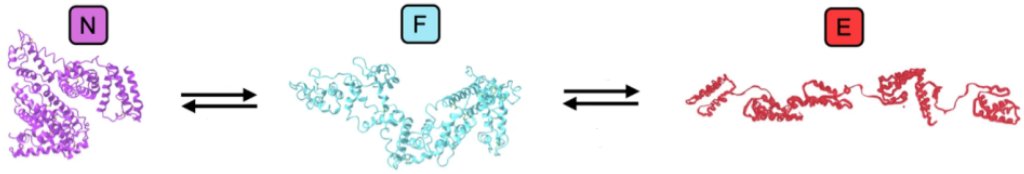

Figure 2.1: Conformational states of BSA: normal (N), fast (F), extended (E). [1]

Under mildly destabilizing conditions (e.g., low pH, mild heat, or weak denaturants), BSA adopts a partially unfolded or folded intermediate, fast (F) state, where inter-domain packing loosens and hydrophobic pockets become more solvent-accessible.

With further stress, BSA progresses to the extended (E) state, where α-helical content is largely lost, domains are fully denatured, and the protein assumes a random coil conformation with exposed hydrophobic surfaces that can promote aggregation. The three states are depicted in Figure 2.1 [64]. These transitions reflect distinct energy minima on the protein's Gibbs free energy landscape, and have been extensively characterized using CD, DSC, fluorescence spectroscopy, and DLS.

The folding and unfolding of BSA can be understood as the outcome of a balance between enthalpic stabilization and entropic driving forces.

On the enthalpic side, strong covalent disulfide bonds in Domain I act as molecular clamps, resisting complete unfolding. Hydrophobic packing across all three domains stabilizes the protein core, while hydrogen bonds preserve the integrity of α-helices and β-sheets. Salt bridges, particularly in Domain II, provide additional electrostatic reinforcement.

On the entropic side, partial or full unfolding increases backbone flexibility and

mobilizes hydrophobic side chains. The release of structured water molecules from previously buried hydrophobic regions further increases solvent disorder, favoring unfolded conformations. These entropic contributions promote conformational heterogeneity, enabling the protein to access a range of structural states.

Taken together, and considering how the energetic contributions vary with temperature, the probabilities of all protein conformations can be predicted at any given temperature, generating an interpretable Boltzmann ensemble.

For BSA, the relevant temperature range for investigation is 0°C to 60°C. The lower bound is set to avoid cold-induced aggregation or solvent freezing, which can artificially constrain conformational sampling. The upper bound remains below the onset of irreversible thermal denaturation [65].

2.3.3.2 Former Work: High temperature study of BSA conformation dynamics using NOT

In recent work by our group, NOT was used to observe a three-state transitional behaviour by invoking localized heating from the incident laser, producing a temperature range of 37 °C to 45 °C [1]. At the various temperatures, the probability density function (PDF) of the incident laser scattering was determined and used to produce a corresponding free energy landscape, a graph of energy across a reaction coordinate that underlies the thermodynamic parameters previously discussed. By evaluating the ΔG of the landscapes, it was concluded that for the N-to-F transition, ΔG had linear temperature dependence, suggesting that it relies mainly on entropy, and can be expressed as:

$$\Delta G(T) = 130 \pm 55 - 0.43T \pm 0.18 \text{ kcal/mol} \tag{2.8}$$

This linear dependence was not observed for the F-to-E transition, however. Rather, a maximum in the change of Gibbs free energy with temperature was observed at 38 °C, a value in agreement with [1], which reported a stability point at 36 °C, while ignoring the N state.

This work was exemplary in analyzing thermodynamic parameters as a conjecture for conformational protein dynamics and stability, as it was relatively untargeted when compared to other label-free analytical methods. It allowed for an unbiased investigation of the entire conformational landscape, since it could be observed for the temperature range probed. However, it did not uncover N-to-F state transition

information as fully as the F-to-E transition, suggesting that a larger temperature range needed to be probed. Therefore, by looking at a lower temperature range, entropic and enthalpic contributions to N-to-F transitions may be rectified. With temperature decrease, enthalpic contributions would dominate and the protein would find a stability maximum for ΔG for the compact N-state. Further, by using BSA as a model system, temperature-controlled NOT for conformational stability analysis can surely be adapted for all proteins, which is the purpose of this thesis.

2.4 Concluding Remarks

This chapter established the theoretical and practical foundation necessary for understanding protein conformational dynamics using thermodynamic principles and NOT. Traditional methods were reviewed for their role in probing protein stability, highlighting both their advantages and limitations. Thermodynamic models, particularly Gibbs free energy, and its refinement through the Gibbs-Helmholtz equation, were introduced as tools for quantifying protein folding behavior across temperature ranges.

A discussion of NOT, which emerged as a unique, label-free platform capable of resolving structural transitions at the single-molecule level was provided. Past work with BSA demonstrated that thermodynamic analysis of laser transmission fluctuations can provide insight into the energy landscape governing protein folding. The extension of this methodology into lower temperature regimes represents a crucial step to achieve a complete characterization of the native and intermediate states of BSA, which is the motivation of the work in this thesis for it also has the potential to demonstrate the broader applicability of NOT for thermodynamic stability analysis of proteins entirely.

Chapter 3

Experimental Methods

This Chapter will outline the methods used in the design and implementation of temperature-controlled NOT experiments. Considerations made to improve a preceding temperature-controlled stage design will be provided followed by the procedures for nanofabrication of DNH gold samples and BSA sample preparation. Then, a suggested protocol to trap single molecules at controlled temperatures is provided, which is an adaptation of the original optical trapping procedure utilized by Dr. Gordon's nanoplasmonic group.

3.1 Temperature-Controlled Stage

3.1.1 Motivation: Previous Temperature-Controlled NOT Experiments

The intention of this thesis was to produce a temperature-controlled stage to fit within a pre-existing optical trapping set-up. It was initially influenced by the previous work of Dr. Elham Babaei, who integrated a thermoelectric cooler (TEC) to reduce the temperature of the gold film during DNH optical trapping of single proteins. Namely, it was shown that the time to trap of BSA was decreased by increasing the voltage of the TEC-system used due to the creation of a thermal gradient with local heating by the incident trapping laser. Further, the corner frequency of trapped BSA and carbonic anhydrase (CA) as a dependency on temperature reduction was under investigation in order to reveal the phenomenological Soret coefficient formulation. However, design parameters, which will be discussed in the following section, resulted

in experimental limitations for future work.

3.1.1.1 Initial Cooling Stage Design

During optical trapping, no external vibrations should be introduced to the optical system, since measurements are mechanically sensitive. In lieu of this, the preceding temperature-controlled stage used a non-mechanical cooling system. Unlike common systems of its type, it did not require fans or fluid to wick away generated heat. It consisted of assembled components on top of a common microscopy slide holder (ThorLabs, MAX3SLH) used in common optical trapping experiments. A solid copper cylinder (3 cm diameter x 4.5 cm length) sat flush against two Peltier TEC coolers (CP2020405H), which were bridged to the sample by a small, "L"-shaped copper piece. All interfaces had thermal grease to increase heat transfer. The Peltier coolers were connected to a DC voltage supply in series, and the temperature was recorded using a hand held infrared temperature gun (Sovarcate, HS960D) directed towards the interface between the copper bridge and the gold sample.

Assuming steady-state conditions and no parasitic losses for this configuration, the theoretical minimum achievable temperature during NOT was $-15.5\,^{\circ}\mathrm{C}$ and the time to achieve it was 3.5 minutes. The heat sink had a heat capacity of 110 J/K. Calculations are presented in Appendix A.1.

3.1.1.2 Limitations of the Previous Experimental Procedure for Cooling during NOT

Despite the theoretical minimum achievable temperature at the cold side of the TEC (sample via the copper bridge), the lowest observed during trapping experimentation was approximately $15.0\,^{\circ}\mathrm{C}$. This was due to the protocol by which data was acquired: the trap was achieved at ambient temperature, then the voltage supply turned on to initiate temperature reduction with the Peltier stack. The rate of cooling was constant and recorded using a cell phone timer at the point of voltage initiation, and matched to a video of the thermal infrared gun values. The time was compared to that of the DAQ for data extraction and analysis. During this time, the rapid rate of cooling on the sample caused the refractive index of the liquid in the solution to change, resulting in a drift in the optical path length within the DNH until the trapped signal was eventually lost within seconds- which is insufficient to achieve the estimated lowest temperature possible at 3.5 minutes. The rate of cooling was

outpaced by the observed thermal drift of the optical system. This inadvertently limited experimental degrees of freedom for common, useful investigative parameters such as power during trapping, and as a result multiple traps would have had to be acquired and compared, introducing nuance during acquisition and variability amongst usable data (ex. DNH selection and alignment, the single molecule being trapped and assessed) and the potential loss of molecular integrity between cooling acquisitions (temperature cycling is typically not recommended during small molecule assessment). In addition, this method imposes limitations on signal analysis due to signal instability. The thermal drift caused by the rapidly decreasing transmission voltage does not allow for long enough usable data segments, despite detrending attempts. Inconsistencies with temperature reporting (since done by hand/eye) were also unideal design outcomes.

3.1.2 Design Considerations for an Improved Temperature-Controlled Stage

This section aims to outline key design considerations made to overcome the limitations previously discussed regarding the initial cooling stage. Improvements focused on: the stage base material, heat sink size and composition, and Peltier stack configuration to increase the overall, stable experimental runtime through a sustained set temperature. The incorporation of a Proportional-Integral-Derivative (PID) controller is then discussed.

The final temperature-controlled stage design comprised: a 3D-printed base, a two-phase heat sink, a three-stage Peltier cooling stack, a copper bridge, and a thermistor connected to a PID controller, as shown in Figure 3.1.

3.1.2.1 3D-Printed Base

The base was a custom 3D-printed rendition of ThorLabs' "MAX3SLH-Microscopy Slide Holder" (Thorlabs, MAX3SLH) that sat on top of the piezoelectric stage (ThorLabs, MDT630B) within the full optical trapping set-up depicted in Figure 3.5. It had 3.0 mm-deep inlays that securely housed other system components to maintain their flush interconnection to optimize heat transfer. The inlays also dampened vibrational noise during optical trapping measurements by securing component positions. The base composition, polyethylene terephthalate glycol (PETG), was selected for its low coefficient of thermal expansion of 0.00006 - 0.00007% per °C increase. PETG's

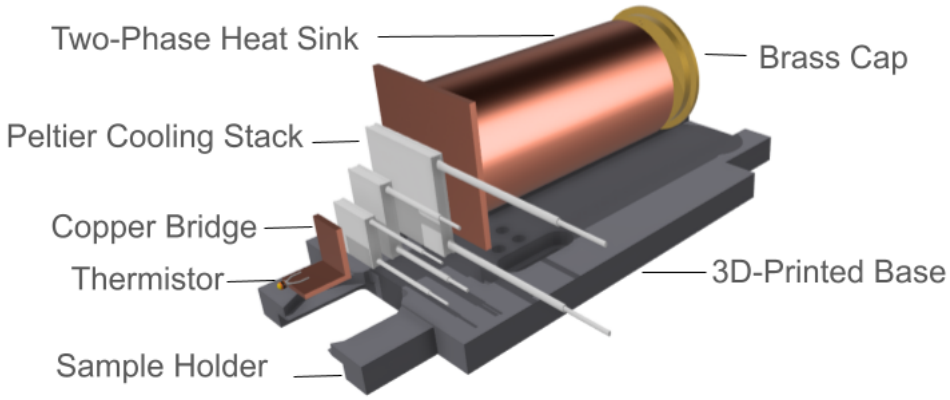

Figure 3.1: Exploded view schematic of temperature-controlled stage.

softening point (80 °C) and high melt temperature (225 − 255 °C) ensured thermal stability throughout operation (the maximum observed temperature of 68 °C) [66]. Compared to other candidate materials (e.g. PLA or ABS), PETG offered higher impact resistance and reduced brittleness. Although PETG is hygroscopic and susceptible to deformation over time under sustained load, these effects were mitigated by limiting the infill of the print to 10% to enhance both structural rigidity and heat dissipation. Since the temperature-controlled stage did not require additional dampening to accommodate fans or fluidics, mechanical robustness was considered less important than thermal resistance. PETG is not reactive to chemicals such as acetone, isopropyl, and ethanol, which are commonly used for cleaning optical set-up components, but can absorb the condensation that inevitably forms during cooling [66]. To preserve the base's mechanical properties the metal components were lined with felt as an absorptive barrier.

3.1.2.2 Two-Phase Heat Sink with Latent Thermal Storage

The previously used cylindrical copper heat sink had a maximum heat capacity of 110 J/K, providing approximately 37.6 minutes of operation for a 38.5 °C temperature difference across the Peltier stack (see Appendices A.1 and A.2). Although increasing the volume of the heat sink could improve this thermal buffer, the design was restricted by spatial limitations once integrated into the entire optical trapping set-up. Specifically, a 52.56 ± 0.02 mm clearance between the stage platform and the optical condenser and the 1 kg maximum load recommended for the piezoelectric stage.

To maximize thermal capacity within these constraints, a two-phase design was

adopted: a copper cylinder with a vented brass cap enclosing a palm–paraffin wax blend (Make Market, 349075). Operationally, the high thermal conductivity of copper (400 W/m·K) facilitated rapid heat transfer from the largest Peltier module to the wax, distributing thermal energy evenly and preventing localized overheating. Once the wax reached its melting point (62.887 °C), its high latent heat of fusion (200–250 J/g) allowed it to absorb incoming heat without a rise in temperature, effectively stabilizing the system [67].

The total thermal storage capacity of the two-phase heat sink was estimated to be $\approx$ 63 kJ, accounting for both sensible heating and the latent heat of the wax, as well as the sensible heat contributions of the copper and brass components. The calculations used $\Delta T = 40°\text{C}$, the temperature difference between ambient conditions and the wax melting point, and are detailed in Appendix A.3. To compare, at this ΔT, the preceding design offers 4.4 kJ in heat storage capacity only; however, this significant improvement needed to be evaluated relative to the total heat load from the Peltier stack in order to assess the operational efficiency of the improved system.

3.1.2.3 Multi-Stage Peltier Cooling Stack

A semiconductive thermocouple made of two materials placed between ceramic plates is a Peltier TEC. With a DC current, p- and n-junctions move in opposing directions, moving heat from one ceramic face to the other, generating a thermal gradient. The performance is quantified by its net cooling power, Q_c, which is defined by:

$$Q_c = \alpha I T_c - \frac{1}{2} I^2 R - K(T_h - T_c) \tag{3.1}$$

where:

Q_c is the cooling power (W),

α is the Seebeck coefficient (V K^{-1}),

I is the electric current (A),

T_c is the cold-side temperature (K),

T_h is the hot-side temperature (K),

R is the electrical resistance (Ω),

K is the thermal conductance (W K^{-1}).

Q_c is influenced by: the Peltier effect (useful cooling caused by heat transport, scaled by the Seebeck coefficient α, which typically ranges from 0.05 to 0.07 V/K for most TEC models), Joule heating (wasted heat due to electrical resistance), and back heat flow (conductive heat transfer from the hot side to the cold side).

System sizing refers to matching the cooling power to the thermal load, Q_L. To achieve this, two parameters are of interest: the maximum cooling capacity, $Q_{\max}$, obtained from the manufacturer's specification sheet, and the temperature difference, ΔT.

Considering the extreme case of maintaining the cold side of the system at 0 °C for one hour, the thermal load was calculated from the maximum heat capacity of the heat sink as:

$$Q_L = \frac{63\,\text{kJ}}{3600\,\text{s}} = 17.5\,\text{W}.$$

Since the heat sink temperature must necessarily be $\approx 63\,^{\circ}\text{C}$ to induce phase change, this value is taken as the temperature difference ΔT. When referring to Figure 3.2 for the largest Peltier module (TEC1-12704), an input current between 3.0 - 4.0 A is required to achieve this ΔT, but it only yields a cooling power Q_C of at most 3 W, which is insufficient to meet the required thermal load of 17.5 W. This relatively low cooling performance is primarily attributed to internal Joule heating within the TEC module itself.

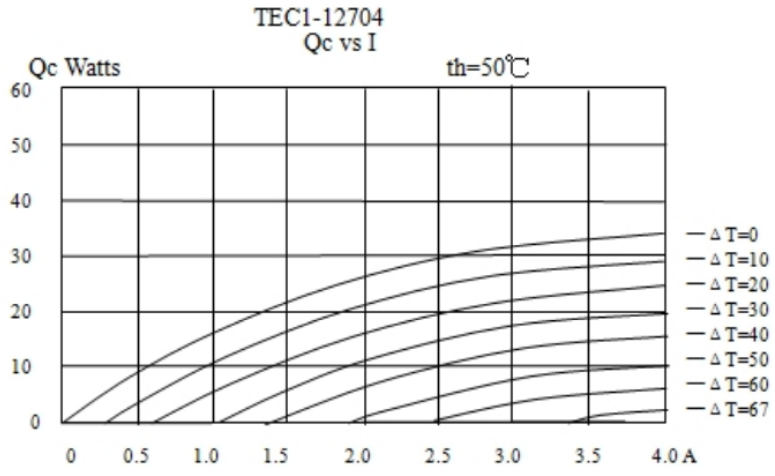

Figure 3.2: Cooling power vs. current for the largest TEC module, TEC1-12704

From Figure 3.2, one can expect a higher Q_C if a lower current is chosen; however, ΔT becomes limited. Stacking multiple Peltier coolers in succession allows the

required ΔT to be split amongst modules. Therefore, in this manner, a three-stage Peltier stack consisting of TEC1-12704K10, TECE-12704K10, and CP2020405H modules was used. The dimensions of each Peltier decreased in size when distanced from the sink, and were arranged pyramidally. The original "L"-shaped copper bridge connected the smallest Peltier cooler to the top of the sample (on the glass side, not the gold side). Thermal grease was used between each element to maximize heat flow within the system.

In the direction of heat flow, each TEC in the stack must dissipate its own internal joule heating and the cumulative heat pumped by all preceding smaller stages. Consequently, the thermal load increased progressively towards the heatsink. To accommodate this, the TEC with the greatest surface area and highest heat-pumping capacity was placed closest to the heatsink since it operates at a relatively low current density when compared to the smaller TECs, thereby reducing resistive (I^2R) losses and preventing thermal bottlenecks that could compromise system stability. Conversely, the smallest TEC was placed closest to the sample, since it was sufficient in handling the lightest thermal load.

The stacked configuration optimized power efficiency: all modules were connected in parallel to the common current supply of the PID, allowing each to draw a fraction of the total current. The parallel connection was preferred since TECs generally exhibit higher efficiency at lower currents. While the cooling power increased linearly with current, the internal joule heating rose quadratically. In this manner, a maximum net cooling point, $I_{\max}$, beyond which additional current causes more heating than cooling, as illustrated in Figure 3.2. Eventually the heating effect surpassed the cooling benefit, so a reasonable operating current was chosen to the left of the global maximum, ensuring net cooling and improved efficiency.

A total input current of 2.0 A was considered. Using the specifications of the TEC modules provided in Table 3.1, the input currents to each module were calculated to be 0.86 A, 0.54 A, and 0.60 A for the CP2020405H, TECE-12704K10, and TEC1-12704K10 modules, respectively. These values all fall on the left-hand side of the net cooling power versus current characteristic curve (i.e., the rising part of the parabola) for each module, according to the manufacturers' datasheets [68, 69, 70]. (See Appendix A.4 for calculation details.)

In Appendix A.5, the total power dissipation of the stack at these currents was calculated to be 14.26 W, which could maintain the lower temperature bound of 0 °C (as the PID set-point) for 73.8 min. This was sufficient for NOT with thermal control.

Table 3.1: Specifications of TEC Modules

TEC Model	Dimensions (mm)	Max Voltage (V)	Max Current (A)	Resistance ()	$Q_{\max}$ (W)
CP2020405H	$20 \times 20 \times 4.05$	6.0	2.0	2.0	7.7 (at $V_{\max}$, 27 °C)
TECE-12704K10*	$30 \times 30 \times 3.6$	15.0	3.0	3.2–3.5	33
TEC1-12704K10	$40 \times 40 \times 4.7$	15.4	4.0 ± 0.5	2.85–3.15	33.4 (at 15.4 V DC)

* Approximated from TEC1-12703 due to lack of datasheet.
** When the ambient temperature changes by 1 °C, the module resistance changes by approximately 0.015 Ω.

3.1.2.4 PID Controller Parameters: Current, Gain, and Steinhart-Hart Constants

For precise temperature control and stability over an experimental time duration of at least one hour, a PID (ILX Lightwave, LDT-5910) controller was used. The temperature feedback was dictated by a negative temperature coefficient (NTC) 10 kΩ thermistor (Amphenol Sensors, TH310J39G), which was affixed to the bridge at the sample end, opposite the smallest Peltier cooler, depicted in Figure 3.1. Considering the thermistor characteristics and the Peltier stack configuration, the PID controller was operated using the following parameters:

Current

According to Section 3.1.2.3 the current was set to 2.0 A as per calculations.

Gain

The analog feedback gain determines how quickly the actual temperature reaches and settles to the set-point value. Counterintuitively, the smallest available gain of 1.0 was used during experimental operation of the temperature-controlled stage, as higher (preprogrammed) gains of 3.0 and above resulted in set-point overshoot followed by prolonged oscillations.

This trade-off was acceptable since the heatsink provided sufficient thermal buffering to meet the experimental time requirement of one hour (73.8 minutes). For example, at a gain of 1.0, the system reached a set-point of 8 °C in approximately 5 minutes, with a maximum overshoot of 0.3 °C, and oscillations that settled after 14 minutes. Reducing the current to 1.8 A did not produce a meaningful improvement in oscillation damping time.

Steinhart-Hart Constants

To account for the non-linear relationship between the thermistor's resistance and temperature, the PID controller was programmed using Steinhart–Hart constants, which were derived using the Steinhart–Hart equation:

$$\frac{1}{T} = A + B\ln(R) + C\left(\ln(R)\right)^3 \tag{3.2}$$

where:

Symbol	Description	Units
T	Temperature	K
R	Resistance	Ω
A	Steinhart–Hart coefficient A	dimensionless
B	Steinhart–Hart coefficient B	dimensionless
C	Steinhart–Hart coefficient C	dimensionless

Three sets of three resistance-temperature pairs were used to calculate A, B, and C, which were then averaged to give the programmable values of $A = 0.0027720$, $B = 0.00025142$, and $C = 2.5648 \times 10^{-7}$. The calculations are in Appendix: A.6.

3.2 Nanofabrication of Gold DNH Samples

Gold DNH sample preparation was initiated with a glass microslide (Fisherbrand 12-550C, $76 \times 25.4 \times 1.0$ mm^3) that was cut into thirds by scribing with a diamond tip and cleaving. The slides were cleaned with 99% ethanol and dried with nitrogen gas. They were then sonicated in ethanol for 10 minutes, followed by sequential rinsing with acetone, deionized water, and ethanol, with drying between each step.

A solution of 1:100 dilution of 300 nm diameter polystyrene beads (Sigma-Aldrich, MFCD00131491 LB3) in 99% ethanol was evenly distributed on the glass slides. The slides were left overnight to allow ethanol evaporation, forming a bead mask with a randomized distribution, including dimers.

The samples were then plasma etched for 170 seconds (Harrick PDC plasma cleaner) to control cusp size then subjected to sputtering of 7 nm of titanium (to form an adhesion layer) followed by 70 nm gold (Mantis QUBE system). Beads were removed by adhesive tape after 10 minutes of sonication in ethanol.

Finally, the samples were cleaned with ethanol, dried with nitrogen gas, cut into quarters using a diamond scribe, and cleaned again. Scanning electron microscopy (Hitachi S-4800) showed that the DNHs had an average aperture length of 471 nm and cusp size of 33 ± 3 nm, suitable for trapping BSA based on its molecular dimensions (provided in Section 2.3.3.1). An example is shown in Figure 3.3.

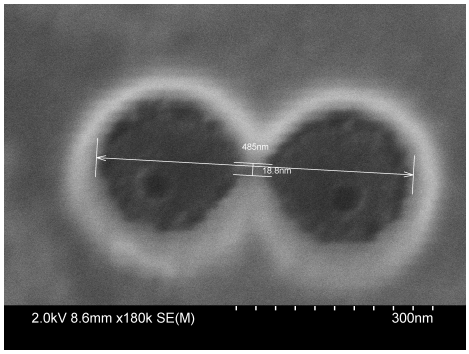

Figure 3.3: Scanning Electron Microscope (SEM) image of a double nanohole (DNH) within a 70nm gold film on glass bound by a 7nm titanium adhesion layer. The length and cusp sizes are displayed.

3.3 Sample Preparation

A 9.4 µL portion of a 10 mg/mL suspension of BSA (Sigma-Aldrich, MWGF70-1KT) in 10 µM phosphate-buffered saline (PBS) was added to a microwell formed by placing a 0.1 mm thick image spacer (Grace BioLabs, GBL-654008-100EA) onto a glass slide (Globe Scientific Inc., 1419-10). The solution was sealed using the DNH sample, with the gold side facing downward.

3.4 Temperature-Controlled NOT

This section aims to outline temperature-controlled NOT. It requires an aptly timed and meticulously orchestrated protocol initiated by the establishment of a stable system temperature, followed by trapping.

3.4.1 Establishment of PID Set-Point Temperature

To estimate the experimental temperature at the center of the microwell, two thermometer probes were placed in addition to the thermistor, as shown in Figure 3.4, and

a cooling trial was performed with the temperature-controlled stage in the absence of an incident laser. Table A.2 in Appendix A.7 provides the coincident temperatures at the thermistor, and probes A and B throughout the duration of the trial.

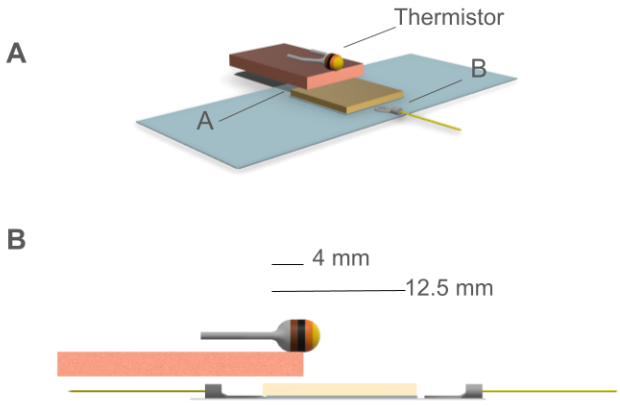

Figure 3.4: Thermistor and probe positions, A and B, on the gold DNH sample during cooling trial (A), and a side view of the sample with dimensions of the gold film (12.5 mm) and bridge-to-sample connection (4.0 mm) (B) used for geometric temperature approximation which assumes a linear temperature gradient across the sample.

In this trial, the PID controller was set to a temperature of 8 °C, which was reached within five minutes, then the system oscillated within 0.4 °C until 14 minutes. The system remained at 8.30 ± 0.03 °C until 58 minutes when it destabilized (the temperature rose in all three probed locations). At thermal equilibrium, it was concluded that the temperatures at A and B were approximately 12.36 ± 0.15 °C and 19.33 ± 0.12 °C.

The temperature at the center of the sample microwell due to cooling, T_C, was estimated geometrically according to Figure 3.4:

$$T_C = \left(\frac{6.25\,\text{mm} - 4\,\text{mm}}{12.5\,\text{mm} - 4\,\text{mm}} \right) (T_B - T_A) + T_A \tag{3.3}$$

$$T_C = 0.2647 \cdot (T_B - T_A) + T_A \tag{3.4}$$

Where T_A and T_B are the equilibrium temperatures measured at probes A and B, respectively.

To consider the temperature contribution from the incident laser due to localized heating during trapping, COMSOL simulation results for a 980 nm laser were assumed, as reported in previous work [1]. This study found a local temperature increase of $0.58\,^{\circ}\mathrm{C\,mW^{-1}}$ of laser power, measured before the objective. A power loss of 25% at 850 nm was assumed as per the manufacturer, and an additional $56.7\% \pm 3\%$ loss through the objective was determined experimentally by comparing power measurements taken before and after the objective using an oil-immersed power meter (Thorlabs, S401, S130VC sensor) (see Table A.3, Appendix A.7), and is referred to as the laser scaling factor (LSF) from this point forward.

Therefore, a generalized equation to calculate the temperature in the microwell, T_M, was deduced:

$$T_M = T_C + \left(0.58\,^{\circ}\mathrm{C\,mW^{-1}} \times \text{Laser Power (mW)} \times \frac{75}{\text{LSF}}\right) \tag{3.5}$$

Substituting the expression for T_C, this becomes:

$$T_M = 0.2647(T_B - T_A) + T_A + \left(\frac{43.5}{\text{LSF}} \times \text{Laser Power (mW)}\right) \tag{3.6}$$

Assuming an LSF value of 43.7, as used in the work presented in this thesis:

$$T_M = 0.2647(T_B - T_A) + T_A + 0.9954 \times \text{Laser Power (mW)} \tag{3.7}$$

The LSF should be recalculated following realignment of the optical set-up since it is alignment-dependent.

3.4.2 Protocol for Experimentation

Once the desired temperature set-point was calculated and programmed along with the operational parameters for the PID controller, the gold DNH sample was mounted onto the temperature-controlled stage. It was critical to establish gentle thermal contact between the underside of the copper bridge and the glass coverslip of the sample—sufficient for efficient heat transfer, but not so tight as to warp or compress the sample, especially during laser focusing and objective alignment. With the sample properly seated, and the incident laser path through the center of the microwell, the PID controller was turned on.

After thermal stabilization at the PID set-point, the 850 nm laser (Eagleyard DFB-0852-00050-BFY02-0002) was activated and aligned to the DNH of the sample. The

laser beam was collimated, passed through a linear polarizer and half-wave plate, and then expanded before entering a 100× oil-immersion microscope objective (1.25 NA, Nikon CFI E Plan Achromat 100× oil). After transmission through the DNH, the beam was collected by a 10× objective (0.25 NA, Olympus Plan N 10×/0.25 FN22), detected by an avalanche photodiode (Thorlabs, APD110A), and digitized via a data acquisition module (Advantech, USB-4711A). A camera was used to assist with DNH visualization and alignment.

Upon protein trapping—identified by a discrete voltage jump and increased noise on the APD signal—the laser current was incremented as needed to achieve specific experimental objectives while the temperature was maintained to within ±0.3°C of the PID set-point. The complete optical trapping setup is shown in Fig. 3.5.

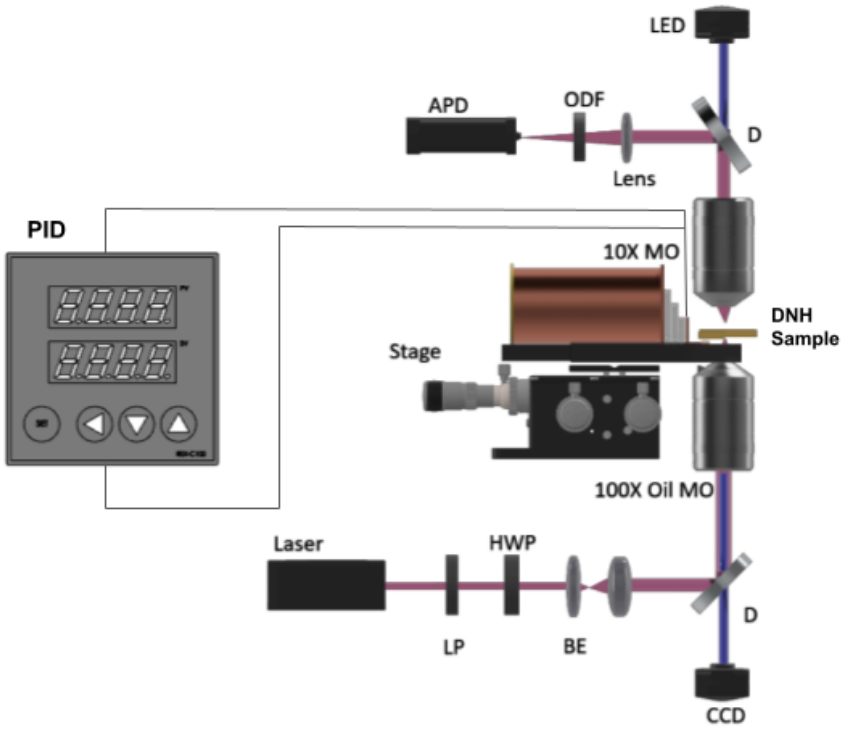

Figure 3.5: Complete temperature-controlled NOT set-up with: PID controller, temperature-controlled stage, and optical trapping components for 850nm laser. The schematic of the NOT setup: DNH sample = gold double nanohole sample, LP = linear polarizer, HWP = half waveplate, BE = beam expander, CCD = charge coupled device, D = dichroic mirror, Oil MO = oil immersion microscope objective, L = lens, ODF = optical density filter, APD = avalanche photodiode.

Chapter 4

Results and Discussion

This chapter provides the results acquired with temperature-controlled NOT. The first section describes observations made using the set-up during preliminary, proof-of-concept experiments, deeming it effective for use in research-based endeavours. The next section presents a study of the conformational transitions of the model protein, BSA, using the temperature-controlled NOT set-up at low temperatures.

4.1 Efficacy of the Temperature-Controlled Stage

Prior to research-intended experiments, the temperature-controlled stage was integrated into an 850 nm optical trapping set-up and evaluated for its efficacy (see Figure 3.5). The signal stability and the accuracy of temperature reporting were considered.

4.1.1 Signal Stability Evaluation

4.1.1.1 Generalized Observation: Previous Temperature Controlled Stage Comparison

This Section compares the general use of the temperature-controlled stage to that of its predecessor discussed in 3.1. As a result of the improved design, a set-point temperature range of 2 °C to 40 °C was achieved, in conjunction with the relevant physiological range for BSA study discussed in Section 2.3.3.1 (since laser heating contributes to the sample temperature). The temperature was sustained over time frames of up to one hour within 0.3 °C of the PID set-point, to accommodate lengthy

experiments.

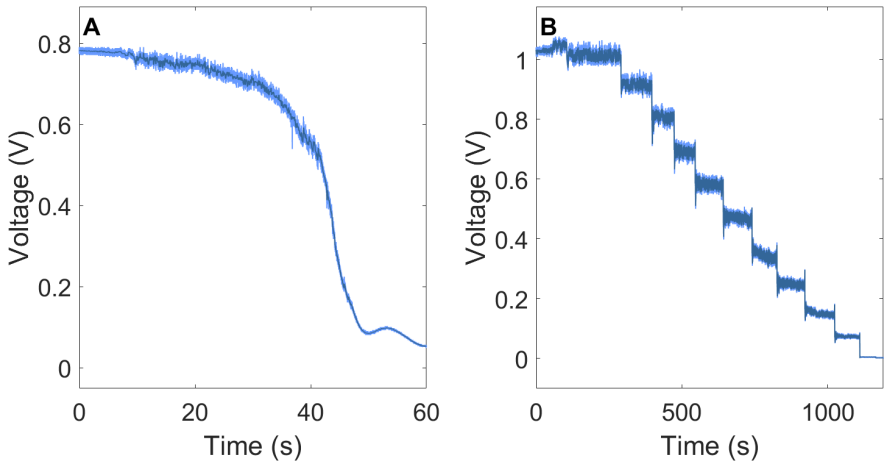

Figure 4.1: Comparison of trapped BSA using two temperature-controlled NOT experimental procedures. In (A), the BSA is trapped at an incident laser current of 130 mA (∼8 mW), then the temperature is reduced using TEC modules. The transmission rapidly decreases linearly around 30 seconds (at 20.36 °C) and is lost by 60 seconds (at 15.27 °C). In (B), the target temperature of 15 °C is reached, then the trap is acquired as before, but is sustained for 1190 s at a PID set-point of 15.0 ± 0.25 °C. The current of the incident laser is reduced in 10 mA (∼0.75 mW) increments until the threshold current of the laser is reached at 30 mA (∼1 mW), allowing experimental flexibility not achievable in (A).

Figure 4.1 compares (A), the initial experimental approach, to (B), the improved procedure, in terms of signal transmission through the DNH over time. Both signals exhibit trapped BSA at 130 mA (∼8 mW) with a 850 nm laser.

In (A), the trap was obtained at ambient temperature (23.22 °C), then the voltage supply to the Peltier coolers was activated to reduce the temperature (see Section 3.1.1.2). The lowest temperature reached was 15.27 °C. The signal and temperature were unstable, causing rapid misalignment through the DNH by 30 seconds (at 20.36 °C), and complete signal loss within one minute. This limits both experiment time and trapping stability.

In (B), the PID set-point temperature was allowed to stabilize before aligning the laser through the DNH. The trap then occurred as in conventional NOT. Temperature stability enabled sustained transmission, allowing for controlled power adjustments - an ideal feature for dynamic experimental approaches. In this example, the laser current was incremented in 10 mA (∼0.75 mW) steps, and the trap was sustained for

1190 s at a PID set-point of 15.0 ± 0.25 °C, nearly 20 times longer than in approach (A).

A sustained horizontal transmission over time is preferred in single-molecule analysis, since a stable molecular state can be identified, making it easier to distinguish between different discrete states or transitions. Flat regions are ideal for quantitative analysis, such as calculating PSD, energy landscapes, or Gaussian fitting, and they align well with modeling techniques such as Hidden Markov Models (HMMs), which assume constant emissions from stable states.

In contrast, a temporally decreasing signal can introduce processing complications. In this temperature-controlled NOT method comparison, the causation of the linear drift in (A) is assumed to be predominantly thermal, which can obscure or mimic molecular conformational transitions, leading to errors in state detection and quantification. For instance, drift can spread out histogram peaks, ultimately undermining the interpretability of the data. It is possible; however, to correct the drift with preprocessing methods such as baseline subtraction (moving average), or polynomial detrending; however, a sustained, flat signal is preferred to avoid overcorrection.

4.1.1.2 Signal to Noise Ratio

A large signal-to-noise ratio (SNR) is preferred during NOT. Factors that enhance SNR include: laser power, since increased power raises both trap stiffness and signal strength; detector sensitivity; and the size and refractive index of the trapped particle relative to the NA geometry.

Detrimental factors to SNR are: laser-induced noise such as power fluctuations and coherence noise; detector-associated thermal and electronic noise; mechanical vibrations within the setup; environmental noise (for example, temperature fluctuations and air currents); artifacts produced by electromagnetic interference from nearby electronic devices; and intrinsic sample noise, including Brownian motion, which is particularly pronounced in low-stiffness traps.

To assess the temperature-controlled stage's influence on SNR, it was calculated for three separate trapping events at ambient according to:

$$\mathrm{SNR} = \left| \frac{\mu_{\mathrm{trap}} - \mu_{\mathrm{baseline}}}{\sigma_{\mathrm{baseline}}} \right| \tag{4.1}$$

where:

μ_{trap} is the mean signal during trapping for 5 seconds,

μ_{baseline} is the mean baseline signal before trapping for 5 seconds,

σ_{baseline} is the standard deviation of the baseline signal.

The average SNR was 24, which is comparable to the reported SNR of 33 for BSA at ambient using conventional NOT by Dr. Gordon's group in [58]. This validates baseline operation of the retro-fitted setup.

During temperature-controlled traps; however, the SNR decreased to 15 at 10 °C and 9 at 16 °C. The reduction is attributed to additional thermal noise introduced by the stage once active. The thermal gradient at the sample sight may cause refractive index changes in the medium that weaken the trap stiffness, and spurious baseline fluctuations arising from convection currents and electronic noise associated with active temperature control. These mechanisms are plausible, but cannot be concluded with certainty without further investigation to isolate the dominant source of SNR degradation (for example, controlled studies with power spectral density).

4.1.2 Temperature Reporting Accuracy

The following figure compares the transmission through the DNH during three high-temperature-controlled trapping events of BSA with symmetrical power incrementation. The PID set-points for the events are: (A) 24.0 °C, (B) 28.0 °C, and (C) 40.0 °C.

During the experiment the ambient room temperature was maintained at 22.0 ± 0.5 °C, and the heat sink was allowed to cool to ambient between each temperature-controlled trapping event. All events were performed using the same gold DNH sample and temperature-controlled trapping performed according to Section 3.4.2.

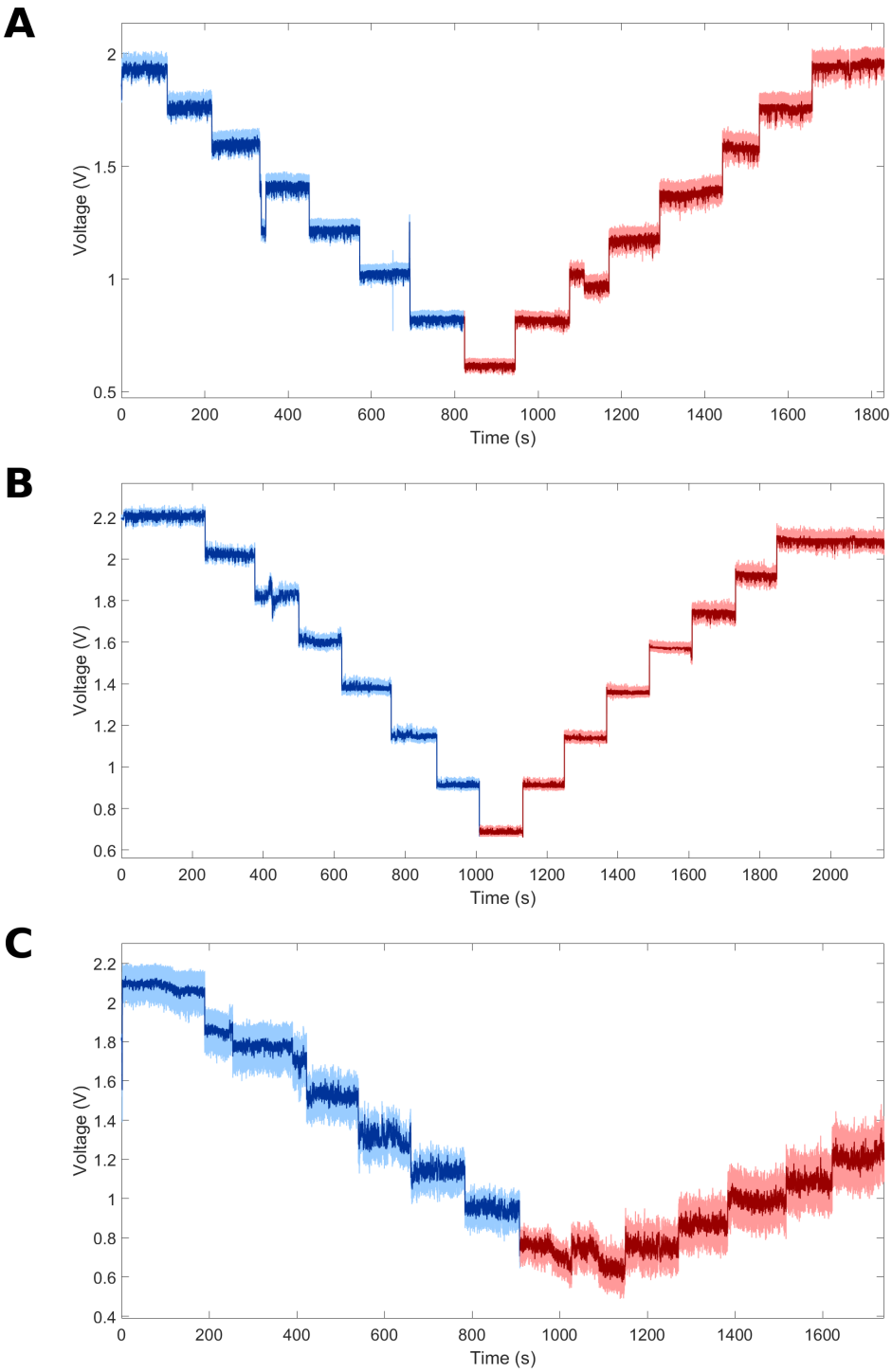

Figure 4.2: Comparison of transmission through the DNH between three high-temperature probed trapping events of BSA with symmetrical power incrementation (14.1, 12.8, 11.8, 10.4, 9.2, 7.9 mW). The PID-set-point temperatures were: (A) 24.0 °C; (B) 28.0 °C; and (C) 40.0 °C. The dissimilar transmission between descending (blue) and ascending (red) arm of each trace suggests thermal hysteresis due to delayed local equilibration of the trapping region, despite constant PID set-points and symmetrical power incrementation during temperature-controlled NOT.

In each trapping event shown in Figure 4.2, the ascending (red trace) power increments do not exactly match their earlier descending (blue trace) counterparts, as expected. Since the PID set-point remains constant during trapping, this behavior suggests thermal lag within the optical trapping system. This discrepancy increased with the PID set-point temperature.

4.1.2.1 Thermal Lag During Power Incrementation

Proper investigation of the thermal lag must consider the same two contributing factors to temperature approximation as in section 3.4.1. The first is localized heating due to light absorption from the incident laser, which increases with power. Lagging heat dissipation within the surrounding medium may cause discrepancy during cooling. The second, a spatio-temporal temperature gradient across the DNH sample, which concerns how its gold-to-glass interface contributes to heat dissipation from the Peltier-stack, akin to the relationship discussed geometrically during low-temperature probing in NOT. Since the perceived thermal lag increased with PID set-point temperature, it was assumed that it was predominantly influenced by the latter, and so was evaluated in the most extreme case of the 40.0 °C PID set-point, from Figure 4.2 (C). In the situation of high-temperature probing; however, the equilibrium was not measured in the same manner as previous to calibrate the true temperature at the DNH of the sample, but rather, a relative approximation using trap stiffness was adopted, which compared an unknown (nominally, at a PID set-point of 40.0 °C) to reference dataset with temperature, T, and using dynamic viscosity, $\mu(T)$, as a proxy:

$$T = 22.82 \pm 0.50\ ^{\circ}\mathrm{C} + \left(0.58\,^{\circ}\mathrm{C\,mW^{-1}} \times \text{Laser Power (mW)} \times \frac{75}{\mathrm{LSF}}\right) \tag{4.2}$$

(See Section 3.4.1.)

For the unknown dataset the stiffness versus power plot is shown below in Figure 4.3, revealing that the stiffness does not follow the same path during downwards (blue trace) as it does during upwards (red trace) power incrementation despite a constant reporting of temperature on the PID-controller. Below that, in Figure 4.4, is the stiffness trend of the reference dataset, which was trapped on the same day, with the same gold DNH sample.

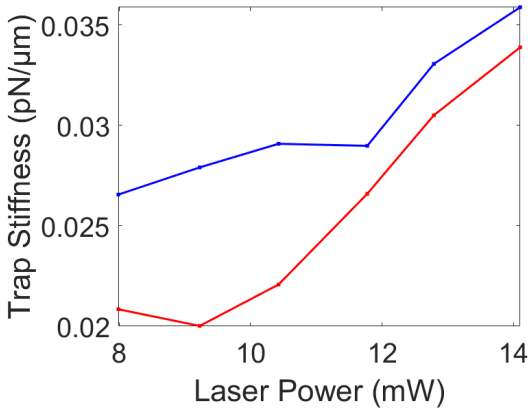

Figure 4.3: Trap stiffness vs. power of trapped BSA at a PID-set point of 40.0 °C. The stiffness is calculated from the corner frequency of the PSD of the signal taken at six powers (14.1, 12.8, 11.8, 10.4, 9.2, 7.9 mW), first through decreasing (blue trace) then increasing incrementation (red trace) during one trapping event with a PID set-point of 40.0 °C. There is discrepancy of stiffness values between each power incrementation arm.

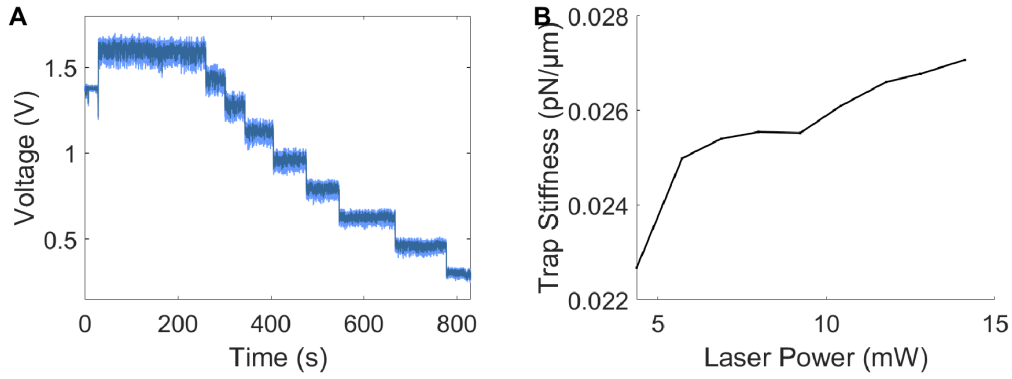

Figure 4.4: (A) Transmission of the ambient temperature trap (reference dataset) through the DNH and (B) Plot of power vs. trap stiffness for the same data set. The ambient temperature was approximated as:
$T = 22.82 \pm 0.50\ ^{\circ}\mathrm{C} + 0.58 \times$ power at the sample, and was used to estimate the temperature for an unknown dataset at the same powers.

At a fixed laser power, trap stiffness $k(T)$ is inversely proportional to the viscosity $\mu(T)$ of the sample medium. The Andrade equation, which describes the exponential decrease of viscosity with temperature for liquids, can be used to model the true local temperature at the DNH at each power in the unknown dataset by comparing the stiffness values to the reference set and applying the inverse relationship:

$$\frac{k_{\text{unknown}}}{k_{\text{ref}}} = \frac{\mu(T_{\text{ref}})}{\mu(T_{\text{unknown}})} \quad \Rightarrow \quad T_{\text{unknown}} = f^{-1}\left(\mu(T_{\text{ref}})\frac{k_{\text{ref}}}{k_{\text{unknown}}}\right) \tag{4.3}$$

where:

$\mu(T)$ is the dynamic viscosity of the liquid at temperature T,

k_{ref} is the trap stiffness at a known reference temperature T_{ref},

k_{unknown} is the stiffness measured at an unknown temperature.

The dynamic viscosity of a liquid can be modeled using the Andrade equation [71]:

$$\mu(T) = A \cdot \exp\left(\frac{B}{T - C}\right) \tag{4.4}$$

where:

A, B, and C are empirical constants specific to the liquid,

T is the temperature in Kelvin.

Here, water is used as an approximation for the sample medium (PBS), with the Andrade coefficients according to [72]:

$$\mu(T) = 2.414 \times 10^{-5} \cdot \exp\left(\frac{247.8}{T - 140}\right) \tag{4.5}$$

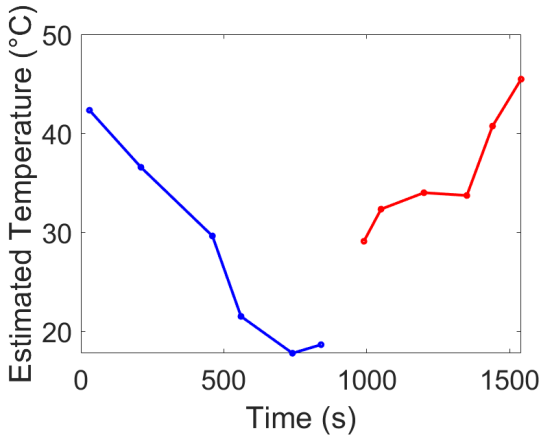

Figure 4.5: Estimated temperature at the DNH sample vs. time during temperature-controlled NOT at high temperatures. The timestamps are taken at the beginning of the corresponding power levels seen in Figure 4.2. The temperature was estimated using trap stiffness and a reference data set for a trap at ambient temperature and by using the Andrade equation, which relates a liquid's viscosity to its temperature. A thermal lag is exemplified, as the red-trace is shifted upwards when compared to its earlier blue-trace counterpart despite symmetrical power incrementation during trapping.

4.1.2.2 Observed Temperature Shifting

It was found that for the trap at a PID set-point of 40.0 °C, the approximated local temperature of the sample per time-stamped power incrementation confirms a spatiotemporal contribution to the local temperature distribution across the gold DNH sample during temperature-controlled NOT at high temperatures. In Figure 4.5, a progressive increase in local temperature is observed over time during identical power increments and is evidenced by the upward shift from the earlier (blue) to the later (red) traces-indicative of thermal lag within the system. This delayed thermal response is expected, as heat originating from the copper bridge must traverse a 1 mm thick glass layer before reaching the thin gold film and subsequently propagating toward the center of the gold DNH sample where trapping occurs, as in the geometric temperature calibration method described in Section 3.4.1. The temperature gradient may be attributed to the substantial disparity in thermal conductivity between the two materials: glass ($\sim$1 $\mathrm{W\,m^{-1}\,K^{-1}}$) acts as a thermal insulator, while gold ($\sim$315 $\mathrm{W\,m^{-1}\,K^{-1}}$) facilitates rapid lateral heat conduction [73]. As a result, the heat transfer process is bottlenecked by the insulating glass substrate, thereby slowing the thermal equilibration across the sample.

It should be discussed; however, the impossibility of reaching approximate temperatures below ambient during high temperature probing, which is exemplified in this analysis. A constant viscosity was approximated to that of water at 23 °C (1.002 mPa s) [72] for all reference, ambient temperatures, not accounting for the dynamic contribution due to local heating of the laser, which would decrease it with increasing power. In addition, the approximation of the corner frequency from the PSD at low laser powers may have been affected by non-Lorentzian behavior, likely arising from system nonlinearities or mechanical drift, as evidenced in Figure 4.2. Such deviations from the ideal Lorentzian profile can introduce significant uncertainty in corner frequency estimation and are more pronounced under weak trapping conditions where SNR is lower and external influences have a greater relative impact. With better attempt; however, this method may be used to approximate the temperature at the sample without probing and employing an arduous geometric approximation such as in section 3.4.1 for calibration.

One further limitation of this approach is that the Andrade equation does not lend to evaluating the distinction between the laser and the Peltier stack contributions to the overall temperature directly. In the expression, the exponential is nonlinear, therefore a decomposition of T is not possible to evaluate, unless one temperature is fixed. The obvious approach would therefore be to assume that the PID set-point is reached instantaneously at the sample, but it has been exemplified here that this is not the case. Alternatively, one can assume the calculation for the laser heating contribution is accurate; however, the COMSOL simulations used were an approximation for a 980nm laser, and assume immediate heat dissipation in the system. This contribution; however, is evidenced during temperature-controlled NOT in Figure 4.2 as the overall trend in heating at the sample is not linear, due to a power dependence.

In summary, when comparing the descending and ascending power ramps, there are observed differences in transmission, trap stiffness, and estimated temperature vs. time, showing a memory effect: the system does not immediately return to the same state when the power is returned. This observation confirms that local sample temperature lags behind power changes due to material thermal resistance, particularly across the glass substrate, and should be accounted for in high-temperature NOT analyses, specifically for temperature calibration. A calibration method that uses a reference (ambient), control dataset was therefore provided.

4.2 Temperature-Controlled NOT at Low Temperatures

This section provides and discusses the experimental results acquired in the publication [74], in which the temperature-controlled NOT presented in this thesis was used to examine the conformational dynamics of BSA at low temperatures (18°C to 25°C). This range was chosen to coincide with the high temperature range investigated by our group [1], thereby covering nearly the entire physiological range relevant to BSA, as discussed in Section 2.3.3.1.

4.2.1 Results

This section will outline the analysis method used to interpret the NOT results found at a PID set-point temperature of 8.0 °C at various powers. Using the temperature calibration outlined in section 3.4.1, at an input current for the 850 nm incident laser of 110 mA, the temperature within the microwell of the sample was estimated to be 21.0 ±1°C. The experimental methods outlined in Chapter 3 were followed, then the current was incremented by 10 mA intervals (corresponding to power intervals of 2 mW), which was interpreted as a 1 °C change due to objective losses and laser heating, in accordance with [1]. The range of temperature was therefore 18.0 ±1°C to 23 ±1°C during a single trapping event.

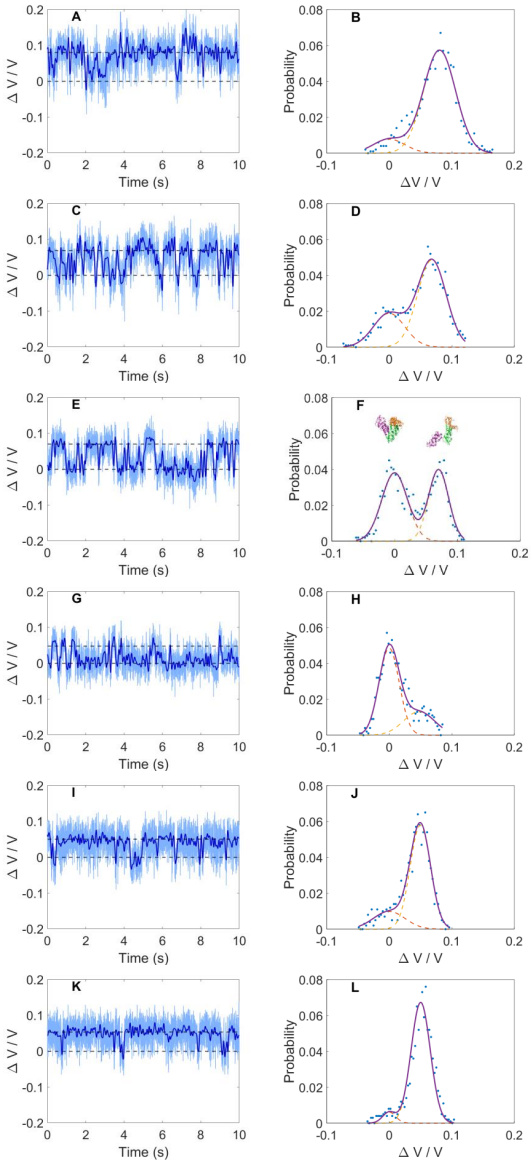

Figure 4.6: The transmission through the DNH nanoaperture due to trapped BSA measured as APD voltage with corresponding PDFs at (A, B) 18 ± 1 °C, (C, D) 19 ± 1 °C, (E, F) 20 ± 1 °C, (G, H) 21 ± 1 °C, (I, J) 22 ±1°C, (K, L) 23 ± 1°C. The voltage levels corresponding to the N and F conformational states are indicated by dashed horizontal lines taken from the mean of Gaussian fits. To allow for comparison at different temperatures, the voltages were normalized by dividing by the voltage of the N-state level (0.4089, 0.5045, 0.5735, 0.6981, 0.8134, and 0.9037 V for 19 ± 1, 20 ± 1, 21 ± 1, 22 ± 1, and 23 ± 1 °C). (F) Ribbon diagrams of the N and F state conformations of BSA are provided as an inset.

The first column in Figure 4.6 shows the observed conformational transitions between the N and F states in the time-series of the APD voltage for six different temperatures during one trapping event. The compactness of the state influences the degree of light scattering, so the N and F states have lower and higher APD transmissions, respectively. The means of which are also provided as horizontal dashed lines in the time-series data. The trapped signal data was acquired at 10 kS/s, and a 100 point average was used to reduce noise. To produce the corresponding probability density functions with double Gaussian fits for each temperature depicted, which are in the second column of the same figure, a 10 s window was binned (N = 50) to ensure both N and F states were captured. The total time for the data presented was 19.5 min; however, the experiment was repeated at eight additional set-point temperatures which had overlapping temperatures with the presented data (based on calibration according to Section 3.4.1 and current incrementation).

The Gaussian fits measured the changes in the transmission intensity due to the conformational changes of BSA, so from the area under each (A_N, A_F), the time spent in each state could be determined. In the aforementioned higher temperature study [1], the probability density was corrected by deconvolution to account for translational, rotational, and other fluctuations of the BSA within the trap. This was required to accurately represent the energy landscape for absolute thermodynamic parameter extraction; however, in this work only the relative occupancy of each state was of interest, so the simple Gaussian fitting procedure was deemed acceptable.

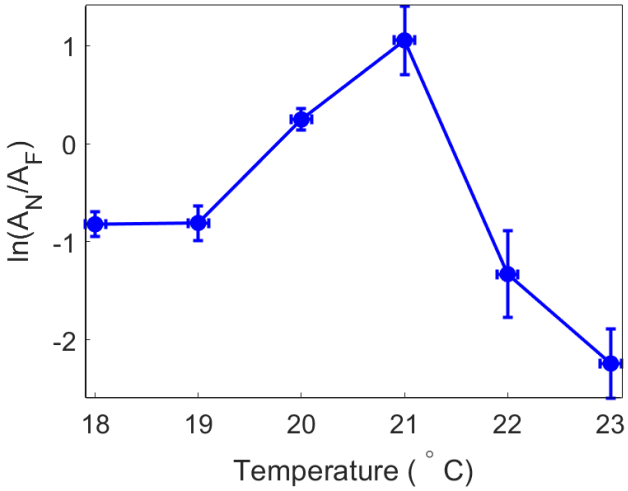

Figure 4.7: The natural logarithm of the ratio between the time spent in each state as described by Arrhenius equation for transition state theory. A maximum was found at 21 ± 1°C, which represents the maximum stability temperature for the compact N form. The temperature error bar was due to the measured fluctuations at the thermistor, and the vertical axis error bar was from uncertainties found by the Gaussian fitting procedure.

To model the relative time spent in each state, Arrhenius' equation was used.

$$\frac{A_N}{A_F} = e^{-\Delta G_{NF}/k_B T} \tag{4.6}$$

where:

A_F is the area (interpreted as time spent) in the folded state,

A_N is the area (interpreted as time spent) in the native state,

ΔG_{NF} is the Gibbs free energy difference between the native and folded states,

k_B is the Boltzmann constant, and

T is the absolute temperature.

In this manner, the change in Gibbs free energy required for conformational state transition can be derived from the natural logarithm of the ratio of the areas, in units of $k_B T$ (and to within a constant offset). A plot of this relative value versus temperature is presented in Figure 4.7. A maximum occurs at 21 ± 1 °C, which was interpreted as the maximum stability point for the N state with respect to the F state.

Circular dichroism measurements reported by [41] suggested that there is a transition at approximately 30.0°C (in 5.0 ± 1 °C steps), likely due to α-helix contributions being replaced with β-sheet contributions. However, this temperature is not comparable to the 21.0 ± 1 °C maximum stability of the N- with respect to the F- state found in this work [74], nor the 36 °C maximum stability expected from Gibbs–Helmoltz theory, nor the 39 °C maximum stability of the E with respect to F state found by [1]. Above 25 °C; however, the onset of the E-state was observed using the temperature-controlled NOT, perhaps indicating that the finding by [41] could also be this. A recent pH study by [75] unveiled that the E form appeared with the observation of β-rich spectra.

4.2.2 Comparative Analysis of Conformational Stability for a Temperature Set

The analysis was repeated for a trap acquired at a low temperature set-point of 11.0 °C with the same DNH sample. Depicted in Figure 4.8 is a maximum stability point observed at approximately 22.0 ± 1 °C, which is within a reasonable range of that reported for the 8.0 °C set-point (21.0 ± 1 °C). The accompanying PDFs and corresponding Gaussian fits are provided in Appendix A.8 for a probed temperature range of 18.0 ± 1 °C to 25.0 ± 1 °C.

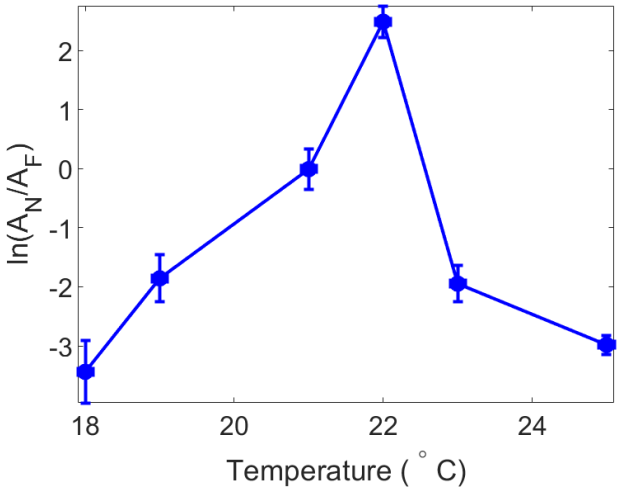

Figure 4.8: Maximum stability temperature for N-to-F state occupancy observed at 22.0 ± 1 °C for a PID set-point temperature of 11.0 ± 0.3 °C, which is within reasonable range of that reported for the 8.0 °C set-point (21.0 ± 1 °C).

Beyond 25.0±1 °C, the E-state was observed, and therefore the relative comparison of N to F state occupancy using Arrhenius' theorem could not be performed.

To quantify the statistical similarity of the conformational state distributions measured at the two temperature data sets, a cross-correlation of the PDFs of the scaled voltage signals was performed. The results are presented as a heat map in Figure 4.9.

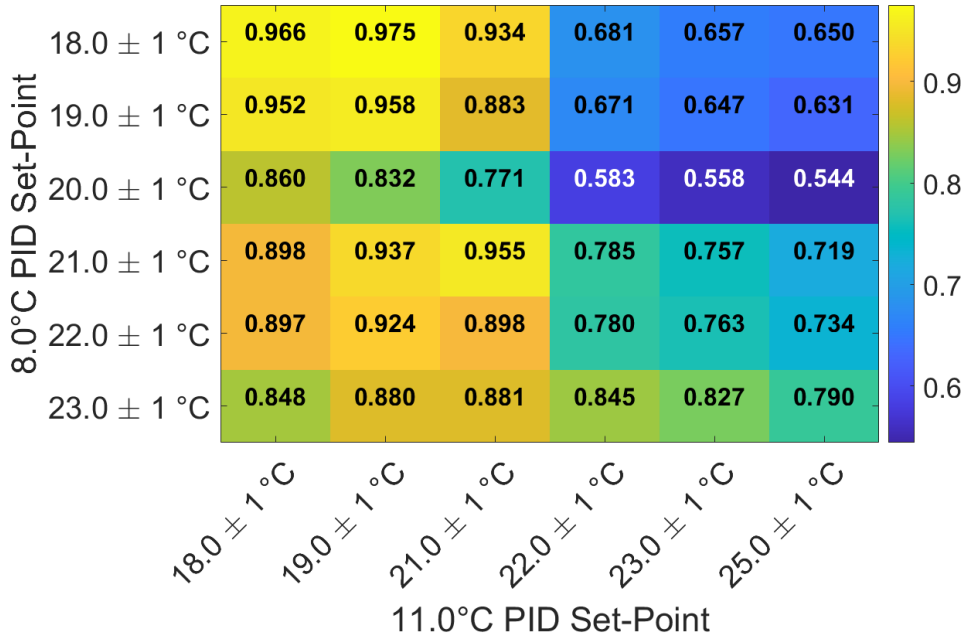

Figure 4.9: Cross-correlation between 8.0 °C and 11.0 °C PID set-point data sets. Dominance at correlating temperature nodes would indicate statistical similarity of conformational state residence times between the two sets, and accuracy in temperature estimation based on 3.4.1.

Ideally, a strong correlation between PDFs measured at corresponding probed temperatures would indicate reproducible temperature-dependent conformational dynamics; however, the heat map exhibits sporadic dominance with multiple off-diagonal peaks. The temperature-dependent PDFs, normalized to their respective N-state mean voltages, are shown in Figure 4.10, with the first dataset at 8.0 °C and 11.0 °C on the bottom. These population distributions reveal a common temperature-dependent trend, which transitions from F- to N- to F-states with increasing temperature, despite inconsistent state occupancy dwell times. Conceptually, this could reflect multiple paths to the same conformational stability point, or alternatively, a variability in the Boltzmann ensemble for the same protein at the same temperature. Since the temporal resolution of 200 µs (accounting for Nyquist and anti-aliasing, with a 10

kHz sampling frequency) of the NOT set-up was sufficient to capture BSA conformational transitions, which have been reported to occur on a millisecond timescale in other temperature-controlled studies over this temperature range [76], histogram results may be skewed from 100-point averaging. States that produce similar optical signatures may have been grouped together, or low-occupancy states may not have been captured.

Furthermore, path-dependent memory may influence behavior: a protein's current state can be biased by its previous state, an effect potentially reinforced by the isolated trapping environment, which lacks *in vivo* factors such as ions, pH variations, or ligand interactions. Additional contributions may arise from laser-induced protein polarity, affecting dipole-dependent conformational features such as α-helices or β-sheets. Without complementary structural methods (CD, NMR, cryo-EM), the precise assignment of states to structural intermediates remains unresolved.

And lastly, inaccuracy in temperature reporting according to the method presented in Section 3.4.1 could contribute to experimental source of error, suggesting refinement.

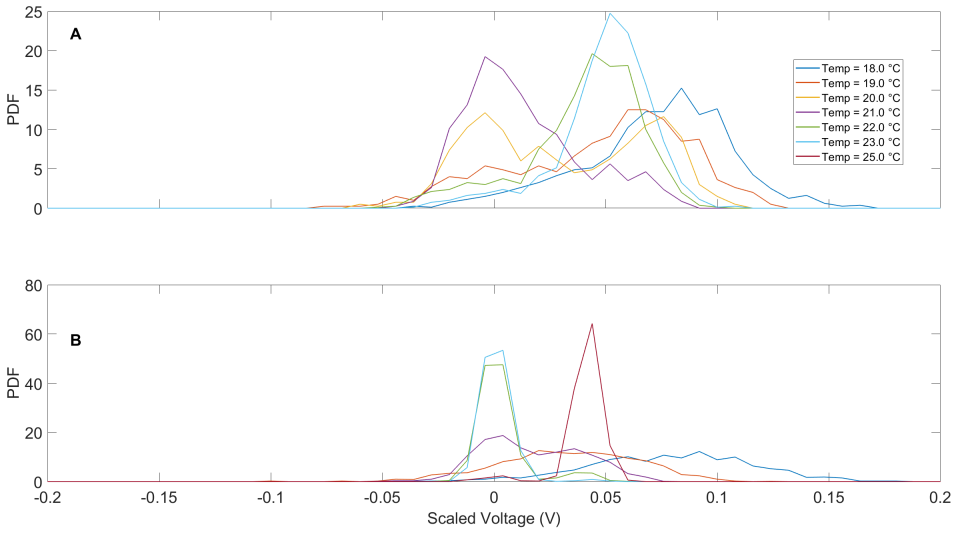

Figure 4.10: Temperature-dependent PDFs of traps at two PID set-point temperatures (8.0 °C (A) and 11.0 °C (B)). The scaled voltage is normalized to the N-state (which is indicated at 0 V). Discrepancies between the two sets may indicate that the conformational ensemble distributions are influenced by independent variables other than temperature during during low-temperature NOT, or that temperature calibration requires refinement.

4.2.3 Conclusion

Using the custom-made temperature-controlled NOT set-up and experimental methods discussed in Chapter 3, this work revealed a conformational stability maximum around 21.0 °C to 22.0 °C, as determined from the relative occupancy of the N-to-F state. This result was reproducible between two traps initiated at different low-temperature PID set-points (8.0 °C and 11.0 °C) within a reasonable range. However, the cross-correlation results highlighted discrepancy in the temperature-dependent statistical distribution of the conformational states between datasets, indicating the need for experimental refinement, specifically in temperature calibration of the gold DNH sample during low-temperature NOT.

Overall, the finding presented in this Section extended prior high-temperature studies by [1] capturing conformational dynamics in a previously unexplored low-temperature regime. It exemplified the value of label-free single-molecule techniques in mapping protein folding landscapes with thermodynamic sensitivity.

Chapter 5

Future Work

5.1 DNH Sample Modification

To address the thermal lag discussed in Section 4.1.2.1, one approach is to reduce the temperature gradient measured across the gold DNH sample during experimentation. Alluding to the disparity between thermal conductivities of the layered materials discussed, a straightforward solution would be to change the point of thermal contact from the glass side to the gold side, allowing heat transfer with the copper bridge to occur directly through the conductive material. However, this cannot be done with the current configuration, since the DNH sample is fixed on top of a microscope slide with an optical spacer, obstructing access to the gold surface from below. Therefore, a design improvement, which is depicted in Figure 5.1, uses a frame made of copper tape, which is applied to microscope slide around the optical spacer. The gold DNH sample is fabricated wider than in the current design, and makes direct contact with the frame, which is connected to the copper bridge forming a continuous conductive path. The 0.5 mm thick glass insulation is bypassed, facilitating symmetrical heat transfer between copper and gold. The high thermal conductivities of the metals may significantly reduce the spatio-temportal thermal gradient, effectively minimizing the observed thermal lag.

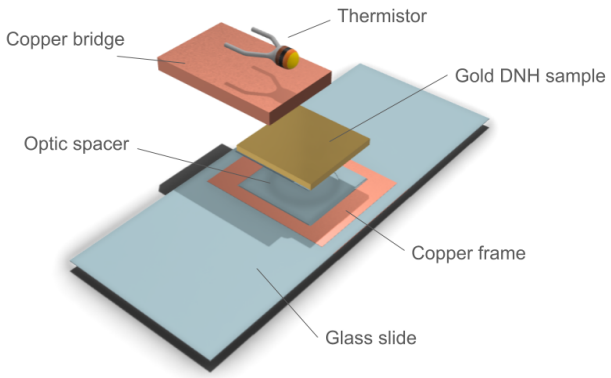

Figure 5.1: Modified DNH sample configuration with a copper tape frame forming a conductive path between the copper bridge of the temperature controlled stage and the gold film. This design bypasses the glass insulating layer to improve heat transfer symmetric and reduce thermal lag during experimentation.

5.2 Temperature-Controlled Stage and Optical Trapping Set-up

The symmetrical heat transfer achieved in the previous section can be improved further by changing the Peltier stack to an annular TEC cooler that rests on top of the sample, allowing light to pass through its center without obstructing the trapping laser's path. To achieve this; however, the optical setup must accommodate a heat sink that can fit between the objective lenses used during transmission mode optical trapping, or reconfigure the setup to reflection mode.

Chapter 6

Conclusions

This work demonstrates a label-free, single molecule platform using DNH optical tweezers with thermal control to probe protein conformational dynamics in real time. Because protein structure is critical to metabolic function and has pathological implications when misfolded or conformationally unstable, understanding folding behaviour under varying conditions is essential. Temperature is key to protein stability, and although thermodynamic parameters such as Gibbs free energy are commonly used, they can be difficult to extract.

To expand upon previous high- temperature studies by this group, this work enables investigation of model protein BSA in a low-temperature regime, revealing a previously unreported conformational stability point of the native, folded (N) state at $21 \pm 1\,^{\circ}\mathrm{C}$. The signal analysis a adopts a relativistic approach based on Arrhenius' theory and state occupancy, allowing a more direct and simplified method to quantify conformational stability and dynamics than previous works that required extensive processing to extract absolute values related to energy landscapes.

This low-temperature stability point has not been uncovered by previous methods, highlighting the invaluable need to explore larger temperature regimes for other proteins in a label-free, unbiased manner.

The novel temperature-controlled stage developed here, which uses a biphasic heat sink, allowed passive thermal modulation of the gold DNH sample while maintaining necessary NOT conditions for experimentation. Temperature calibration techniques and suggestions for design improvements are provided to encourage future exploration of thermodynamic parameters of single molecules.

Appendix A

Additional Information

A.1 Initial Cooling Stage Design: Minimum Achievable Temperature and Experimental Time

The system includes:

Two CP2020405H thermoelectric coolers (TECs):

- Connected in series to a 2 V power supply.
- Maximum temperature difference: $\Delta T_{\max} \approx 77°\text{C}$
- Maximum current: $I_{\max} \approx 2.0\,\text{A}$
- Internal resistance: $R \approx 2.0\,\Omega$

A copper L-shaped bridge:

- Dimensions: length = 5 cm, width = 2 cm, height = 0.3 cm
- Specific heat capacity: $c_p = 0.385\,\text{J/g·K}$
- Density: $\rho = 8.96\,\text{g/cm}^3$

Ambient temperature: $T_{\text{amb}} = 23°\text{C}$

TEC Operational Parameters

For one TEC, at 1 V input:

$$I = \frac{V}{R} = \frac{1}{2.0} = 0.5\,\text{A}$$

This gives a relative current:

$$I_r = \frac{I}{I_{\max}} = \frac{0.5}{2.0} = 0.25$$

Assuming the cooling capability of the TEC scales linearly with current at low currents ($\Delta T \propto I$), the temperature change can be estimated as:

$$\Delta T \approx 0.25 \cdot 77 = 19.25^\circ\text{C}$$

The cascaded temperature difference across two stacked TEC modules is therefore:

$$T_{\text{hot}} = 23^\circ\text{C}, \quad \Delta T = 19.25^\circ\text{C}$$

$$\Rightarrow T_{\text{cold}} = 23^\circ\text{C} - 2 \times 19.25^\circ\text{C} = -15.5^\circ\text{C}$$

Thus, the minimum achievable temperature at this voltage is:

$$\boxed{T_{\min} \approx -15.5^\circ\text{C}}$$

To estimate the time required to cool the sample via the copper bridge, the cooling power of the adjacent TEC must be considered under the specified operating conditions. According to the manufacturer's specification sheet, at an input voltage of 1 V and a temperature difference of $\Delta T = 19.25^\circ$C, the cooling power is $Q_c \approx 0.95$ W.

The copper bridge has:

$$\text{Volume:} \quad V = 5 \cdot 2 \cdot 0.3 = 3\,\text{cm}^3$$

$$\text{Mass:} \quad m = 3 \cdot 8.96 = 26.88\,\text{g}$$

Then, its heat capacity is:

$$C = m \cdot c_p = 26.88 \cdot 0.385 \approx 10.35\,\text{J/K}$$

To estimate the cooldown time:

$$\Delta t = \frac{C \cdot \Delta T}{Q} = \frac{10.35 \cdot 19.25}{0.95} \approx 209.7\,\text{seconds} \approx 3.5\,\text{minutes}$$

The time to reach $-15.5°\text{C}$ is:

$$\boxed{\text{Cooldown time} \approx 3.5\,\text{minutes}}$$

A.2 Thermal Buffer Estimate of Copper Heatsink

The copper heatsink is a solid cylinder with:

Diameter: $3\,\text{cm}$

Length: $4.5\,\text{cm}$

A solid cylindrical copper heatsink:

Dimensions: diameter $= 3\,\text{cm}$, length $= 4.5\,\text{cm}$

Specific heat capacity: $c_p = 0.385\,\text{J/g·K}$

Density: $\rho = 8.96\,\text{g/cm}^3$

Volume and Mass

$$V = \pi r^2 h = \pi \left(\frac{3}{2}\right)^2 \cdot 4.5 = \pi \cdot 2.25 \cdot 4.5 \approx 31.8\,\text{cm}^3$$

$$m = V \cdot \rho = 31.8 \cdot 8.96 \approx 285\,\text{g}$$

Thermal Capacity

$$c_p = 0.385\,\text{J/g·K} \Rightarrow C = m \cdot c_p = 285 \cdot 0.385 \approx 110\,\text{J/K}$$

Estimated Hold Time

Assuming the heatsink absorbs a thermal load of:

$$Q_{\text{load}} \approx 2 \times 0.95\,\text{W} \quad \text{(from two TECs operting at 1 V input each)}$$

The time before reaching thermal saturation is:

$$\Delta t = \frac{C \times \Delta T}{Q_{\text{load}}} = \frac{110 \times 19.5 \times 2}{1.9} = 2257.89\,\text{seconds} \approx 37.63\,\text{minutes}$$

$$\boxed{\text{Time at thermal saturation: } \approx 37.63\,\text{minutes}}$$

A.3 Thermal Storage Capacity of Two-Phase Heat Sink

The composite heat sink consists of three main materials: copper, brass, and a palm-paraffin wax blend. Their volumes, masses, and thermal properties are calculated as follows:

Volume and Mass Calculations

Copper Wall Volume:

$$\begin{aligned} V_{\text{wall}} &= \pi(r_{\text{outer}}^2 - r_{\text{inner}}^2) \times L \\ &= \pi(2.7^2 - 2.58^2) \times 9.25 \\ &= \pi(7.29 - 6.6564) \times 9.25 \\ &= \pi \times 0.6336 \times 9.25 \\ &= 18.41\,\text{cm}^3 \end{aligned}$$

Copper Base Volume:

$$\begin{aligned} V_{\text{base}} &= \text{Length} \times \text{Width} \times \text{Height} \\ &= 5.747 \times 5.747 \times 0.25 \\ &= 8.26\,\text{cm}^3 \end{aligned}$$

Brass Cap Volume:

$$\begin{aligned} V_{\text{cap}} &= \pi r^2 h \\ &= \pi \times (2.9025)^2 \times 0.207 \\ &= 5.48\,\text{cm}^3 \end{aligned}$$

Inner Wax Volume:

$$\begin{aligned} V_{\text{cap}} &= \pi r^2 h \\ &= \pi \times (2.58)^2 \times 9.25 \\ &= 193.43\,\text{cm}^3 \end{aligned}$$

Mass Calculations:

$$m_{\text{wall}} = V_{\text{wall}} \times \rho_{\text{Cu}} = 18.41 \times 8.96 = 164.96\,\text{g}$$
$$m_{\text{base}} = V_{\text{base}} \times \rho_{\text{Cu}} = 8.26 \times 8.96 = 74.03\,\text{g}$$
$$m_{\text{cap}} = V_{\text{cap}} \times \rho_{\text{Brass}} = 5.48 \times 8.44 = 46.26\,\text{g}$$
$$m_{\text{Wax}} = V_{\text{Wax}} \times \rho_{\text{Wax}} = 193.43 \times 0.90 = 174.09\,\text{g}$$

Heat Capacities

Using specific heat capacities c_p from literature:

Copper: $c_p = 0.385\,\text{J/g·K}$

Brass: $c_p = 0.380\,\text{J/g·K}$

Wax (paraffin): $c_p = 2.1\,\text{J/g·K}$

Calculating heat capacity $C = m \cdot c_p$:

$$C_{\text{Cu}} = 238.99 \times 0.385 = 92.01\,\text{J/K}$$
$$C_{\text{Brass}} = 46.24 \times 0.380 = 17.57\,\text{J/K}$$
$$C_{\text{wax}} = 174.09 \times 2.1 = 365.589\,\text{J/K}$$

$$\boxed{C_{\text{total sensible}} = 92.01 + 17.57 + 365.589 = 475.17135\,\text{J/K}}$$

Latent Heat of Wax

The paraffin wax undergoes a phase change near 63°C with a latent heat of fusion of approximately 250 J/g:

$$Q_{\text{latent}} = 174.09 \times 250 = 43,522.50\,\text{J}$$

Total Thermal Storage

Assuming a temperature swing $\Delta T = 40$°C (from ambient to phase change temperature), the total energy stored including latent heat is:

$$Q_{\text{total}} = C_{\text{total sensible}} \times \Delta T + Q_{\text{latent}} = 475.17135 \times 40 + 43,522.50 = 62,529.354\,\text{J}$$

A.4 Current Distribution Across Peltier Stack

For a total input current of $I_{\text{total}} = 2.0\,\text{A}$, connected in parallel, the current per Peltier module is calculated as follows:

Resistances:

CP2020405H: $R_{\text{CP}} = 2.0\,\Omega$

TECE-12704K10: $R_{\text{TECE}} = 3.2\,\Omega$

TEC1-12704K10: $R_{\text{TEC1}} = 2.85\,\Omega$

Voltage:

For each TEC under a common unknown voltage V:

$$I_{\text{total}} = I_{\text{CP}} + I_{\text{TECE}} + I_{\text{TEC1}} = 0.5V + 0.3125V + 0.3509V = 1.1634V = 2.0\,\text{A}$$

$$\Rightarrow \quad V \approx \frac{2.0}{1.1634} \approx 1.719\,\text{V}$$

Peltier Module Current Distribution:

$$I_{\text{CP}} = \frac{1.719}{2.0} = 0.8595\,\text{A}$$
$$I_{\text{TECE}} = \frac{1.719}{3.2} \approx 0.5372\,\text{A}$$
$$I_{\text{TEC1}} = \frac{1.719}{2.85} \approx 0.6032\,\text{A}$$

The current distributed to each module is:

CP2020405H (20×20mm): $\boxed{0.86\,\text{A}}$

TECE-12704K10 (30×30mm): $\boxed{0.54\,\text{A}}$

TEC1-12704K10 (40×40mm): $\boxed{0.60\,\text{A}}$

A.5 Operational Efficiency of Peltier Stack

Power Dissipation Calculation for Each Module:

Power Dissipation per TEC

CP2020405H

At $I = 0.86\,\text{A}$, the approximate power dissipation is estimated based on the maximum rating of $7.7\,\text{W}$ at $2.0\,\text{A}$. Assuming linear scaling with current:

$$P_{\text{CP2020405H}} = \frac{0.86}{2.0} \times 7.7\,\text{W} = 3.31\,\text{W}$$

TECE-127004K10

$$P_{\text{TECE-127004K10}} = \frac{0.54}{2.0} \times 33\,\text{W} = 5.94\,\text{W}$$

TEC1-127004K10

$$P_{\text{TEC1-127004K10}} = \frac{0.6}{4.0} \times 33.4\,\text{W} = 5.01\,\text{W}$$

Total Power Dissipation

$$P_{\text{total}} = 3.31\,\text{W} + 5.94\,\text{W} + 5.01\,\text{W} = 14.26\,\text{W}$$

Time to Reach Thermal Saturation

Assuming a thermal load of $63\,\text{kJ}$:

$$t = \frac{63,000\,\text{J}}{14.26\,\text{W}} = 4421.18\,\text{s}$$

$$t = \frac{4421.18\,\text{s}}{60\,\text{s/min}} \approx 73.83\,\text{min}$$

A.6 Steinhart-Hart Constants

The Steinhart–Hart constants were calculated using three sets of temperature–resistance pairs as provided by the manufacturer. The results from each set, as well as their average, are listed below.

Table A.1: Temperature-Resistance Pairs for thermistor Steinhart-Hart Coefficient Fits for Different Data Ranges

Set	**Data Points (T, R)**	A	B	C
1	$(-40, 341.2)$, $(25, 10)$, $(150, 0.194)$	0.0027747	0.00025013	2.8×10^{-7}
2	$(-10, 55.76)$, $(0, 32.82)$, $(35, 6.528)$	0.0027708	0.00025196	2.4838×10^{-7}
3	$(-2, 36.39)$, $(10, 19.95)$, $(25, 10)$	0.0027704	0.00025217	2.4106×10^{-7}
Average	–	**0.0027720**	**0.00025142**	$\mathbf{2.5648 \times 10^{-7}}$

According to the manufacturer, Equation (3.2) yields a maximum error of 0.01 °C over the range −20 °C to 50 °C.

A.7 Establishment of PID Set-Point

Table A.2: Temperature vs. time measured at three probes on the gold DNH sample: T_{therm}, Probe A, and Probe B. Thermal equilibrium is reached and maintained from approximately 14 to 58 minutes, at temperatures: $T_{therm} = 8.30 \pm 0.03$ °C, $T_A = 12.36 \pm 0.15$ °C, and $T_B = 19.33 \pm 0.12$ °C.

Time (min)	$\mathbf{T_{therm}}$ **(°C)**	$\mathbf{T_A}$ **(°C)**	$\mathbf{T_B}$ **(°C)**
0.00	22.8	22.8	22.7
19.97	20.47	22.7	22.6
28.58	18.36	22.1	22.6
37.37	16.48	21.6	22.5
44.64	15.29	21.1	22.5
53.75	14.10	20.5	22.4
62.17	13.22	19.8	22.3
69.85	12.65	19.3	22.2
77.84	12.92	18.8	22.1
83.70	12.21	18.3	22.1
95.90	11.57	17.7	21.9
111.25	10.78	16.7	21.5

Continued on next page

Table A.2 – *Continued from previous page*

Time (min)	**T_{therm} (°C)**	**T_A (°C)**	**T_B (°C)**
127.48	10.09	16.0	21.1
147.50	9.33	15.1	20.9
179.32	8.74	14.1	20.4
220.90	8.28	13.3	19.9
320.60	8.01	12.1	19.2
559.27	8.13	12.3	19.3
840.96	8.31	12.0	19.2
985.50	8.26	12.1	19.2
1140.64	8.28	12.3	19.5
1440.71	8.34	12.2	19.1
1740.98	8.27	12.3	19.4
2040.56	8.29	12.4	19.4
2341.64	8.32	12.5	19.3
2648.10	8.25	12.5	19.2
2941.10	8.33	12.5	19.4
3240.64	8.34	12.4	19.5
3539.88	8.36	12.4	19.2
3842.19	9.03	12.6	19.5
4149.56	9.17	12.8	19.7

Table A.3: Calculation of the laser scaling factor (LSF), which is the mean of the ratios of power before and after the objective measured at 10 mW increments of the 850 nm laser current. The laser has a threshold of 30 mW, and at this alignment, LSF = 43.7.

Current (mA)	**Power After Objective (mW)**	**Power Before Objective (mW)**	**Ratio (After/Before)**
30	1.12	1.11	1.009
40	1.78	3.41	0.522
50	2.53	5.63	0.449
60	3.14	7.96	0.394
70	3.81	10.35	0.368
80	4.51	12.78	0.353
90	5.26	12.35	0.426
100	5.91	17.76	0.333
110	6.43	20.54	0.313
120	7.47	22.84	0.327
130	7.97	25.52	0.312
Average			**0.437**

A.8 Gaussian Fits for PID-Set Point of $11.5 \pm 0.3\,^{\circ}\mathrm{C}$

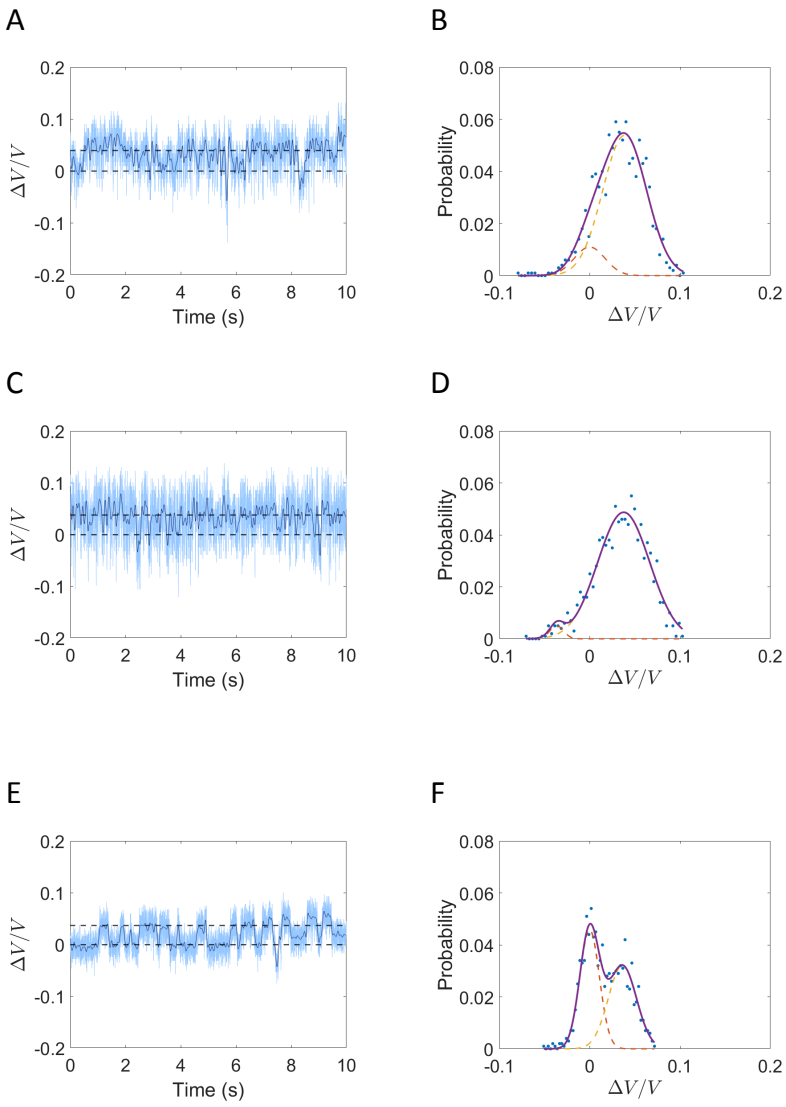

Figure A.1: Figure continued onto next page.

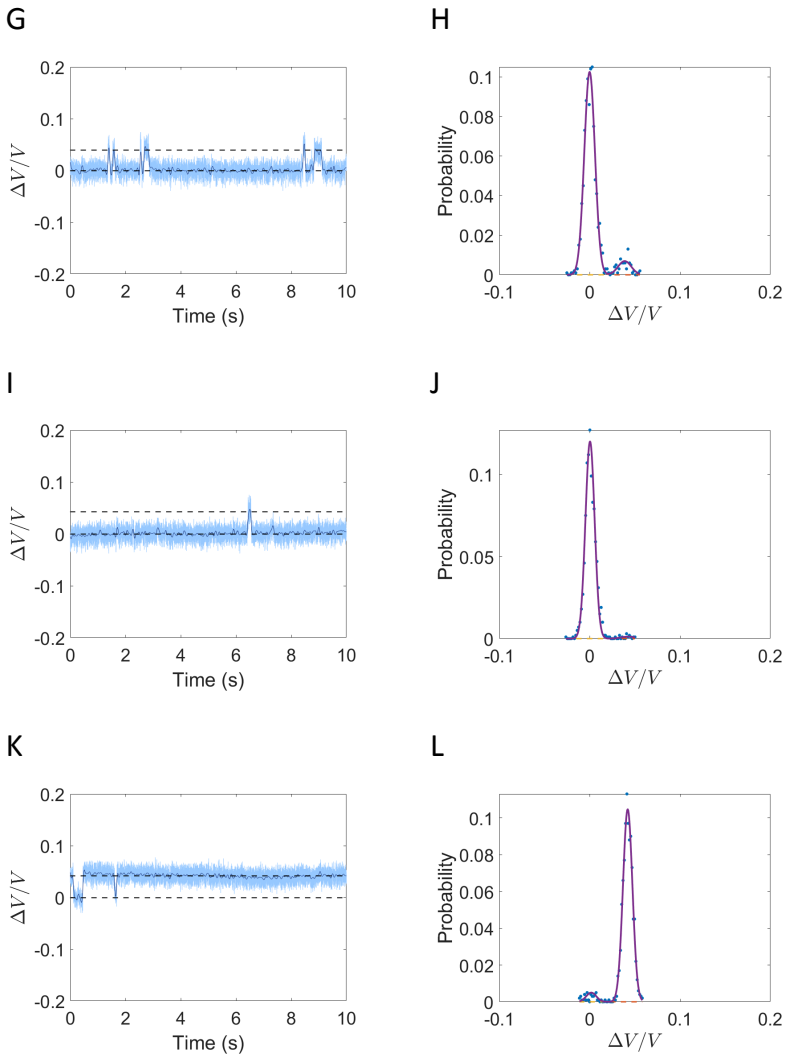

Figure A.2: (A) APD voltage measuring transmission through the DNH aperture with BSA trapped and corresponding PDFs at (A, B) 18 ± 1 °C, (C, D) 19 ± 1 °C, (E, F) 21 ± 1 °C, (G, H) 22 ± 1 °C, (I, J) 23 ±1°C, (K, L) 25 ± 1°C. The N and F levels are indicated by dashed horizontal lines taken from the mean of Gaussian fits. The voltages were normalized to allow comparison at different temperatures by dividing through by the voltage of the N-state level (0.2450, 0.3292, 0.6656, 0.8820, 0.9945, 1.2078 V for 18 ± 1, 19 ± 1, 21 ± 1, 22 ± 1, 23 ± 1 °C, and 25 ± 1 °C).

Bibliography

[1] M. Peters, T. Zhao, S. George, V. G. Truong, S. N. Chormaic, C. Ying, R. A. Nome, and R. Gordon, "Energy landscape of conformational changes for a single unmodified protein," *npj Biosensing*, vol. 1, p. 14, 2024.

[2] G. Zhang, M. J. Leibowitz, P. J. Sinko, and S. Stein, "Multiple-peptide conjugates for binding β-amyloid plaques of alzheimer's disease," *Bioconjugate Chemistry*, vol. 14, no. 1, pp. 86–92, 2003.

[3] S. Zhu, D. Bäckström, L. Forsgren, and M. Trupp, "Alterations in self-aggregating neuropeptides in cerebrospinal fluid of patients with parkinsonian disorders," *Journal of Parkinson's Disease*, vol. 12, no. 4, pp. 1169–1189, 2022.

[4] M. Jimenez-Sanchez, F. Thomson, E. Zavodszky, and D. Rubinsztein, "Autophagy and polyglutamine diseases," *Progress in Neurobiology*, vol. 97, no. 1, pp. 67–82, 2012.

[5] L. C. Walker, H. LeVine, M. P. Mattson, and M. Jucker, "Inducible proteopathies," *Trends in Neurosciences*, vol. 29, no. 9, pp. 438–443, 2006.

[6] A. Mukherjee and C. Soto, "Prion-like protein aggregates and type 2 diabetes," *Cold Spring Harbor Perspectives in Medicine*, vol. 7, no. 3, p. a024315, 2017.

[7] L. M. Blancas-Mejía and M. Ramírez-Alvarado, "Systemic amyloidoses," *Annual Review of Biochemistry*, vol. 82, pp. 745–774, 2013.

[8] A. Bhattacharya and U. Chatterji, "Exosomal misfolded proteins released by cancer stem cells: dual functions in balancing protein homeostasis and orchestrating tumor progression," *Discover Oncology*, vol. 15, no. 1, p. 392, 2024.

[9] S. N. Gummadi, "What is the role of thermodynamics on protein stability?," *Biotechnology and Bioprocess Engineering*, vol. 8, pp. 9–18, 2003.

[10] G. Bruylants, J. Wouters, and C. Michaux, "Differential scanning calorimetry in life science: Thermodynamics, stability, molecular recognition and application in drug design," *Current Medicinal Chemistry*, vol. 12, no. 17, pp. 2011–2020, 2005.

[11] W. J. Becktel and J. A. Schellman, "Protein stability curves," *Biopolymers*, vol. 26, pp. 1859–1877, 1987.

[12] E. Vuorinen, S. Valtonen, V. Eskonen, T. Kariniemi, J. Jakovleva, K. Kopra, and H. Härmä, "Sensitive label-free thermal stability assay for protein denaturation and protein–ligand interaction studies," *Analytical Chemistry*, vol. 92, no. 5, pp. 3512–3516, 2020.

[13] N. Gooran and K. Kopra, "Fluorescence-based protein stability monitoring—a review," *International Journal of Molecular Sciences*, vol. 25, no. 3, p. 1764, 2024.

[14] K. E. S. Tang and K. A. Dill, "Native protein fluctuations: The conformational-motion temperature and the inverse correlation of protein flexibility with protein stability," *Journal of Biomolecular Structure and Dynamics*, vol. 16, no. 2, pp. 397–411, 1998.

[15] A. K. Dunker, J. D. Lawson, C. J. Brown, R. M. Williams, P. Romero, J. S. Oh, C. J. Oldfield, A. M. Campen, C. M. Ratliff, K. W. Hipps, J. Ausió, M. S. Nissen, R. Reeves, C. Kang, C. R. Kissinger, R. W. Bailey, M. D. Griswold, W. Chiu, E. C. Garner, and Z. Obradovic, "Intrinsically disordered protein," *Journal of Molecular Graphics and Modelling*, vol. 19, no. 1, pp. 26–59, 2001.

[16] M. R. Ajmal, "Protein misfolding and aggregation in proteinopathies: Causes, mechanism and cellular response," *Diseases*, vol. 11, no. 1, p. 30, 2023.

[17] K. A. Markossian and B. I. Kurganov, "Protein folding, misfolding, and aggregation. formation of inclusion bodies and aggresomes," *Biochemistry (Moscow)*, vol. 69, pp. 971–984, 2004.

[18] A. Ciechanover, "The ubiquitin proteolytic system: From a vague idea, through basic mechanisms, and onto human diseases and drug targeting," *Neurology*, vol. 66, no. Suppl 1, pp. S7–S19, 2006.

[19] M. Zaman, A. N. Khan, S. M. Zakariya, and R. H. Khan, "Protein misfolding, aggregation and mechanism of amyloid cytotoxicity: An overview and therapeutic strategies to inhibit aggregation," *International Journal of Biological Macromolecules*, vol. 134, pp. 1022–1037, 2019.

[20] S. J. Shire, "Formulation and manufacturability of biologics," *Current Opinion in Biotechnology*, vol. 20, pp. 708–714, 2009.

[21] L. G. Korotchkina, K. Ramani, and S. V. Balu-Iyer, "Folding considerations for therapeutic protein formulations," *Progress in Molecular Biology and Translational Science*, vol. 83, pp. 255–270, 2008.

[22] P. J. Carter, "Introduction to current and future protein therapeutics: A protein engineering perspective," *Experimental Cell Research*, vol. 317, pp. 1261–1269, 2011.

[23] H. S. Samra and F. He, "Advancements in high throughput biophysical technologies: Applications for characterization and screening during early formulation development of monoclonal antibodies," *Molecular Pharmaceutics*, vol. 9, pp. 696–707, 2012.

[24] E. L. Snapp and R. S. Hegde, "Rational design and evaluation of fret experiments to measure protein proximities in cells," *Current Protocols in Cell Biology*, vol. 32, pp. 17.19.11–17.19.20, 2006.

[25] J. A. Broussard and K. J. Green, "Research techniques made simple: Methodology and applications of förster resonance energy transfer (fret) microscopy," *Journal of Investigative Dermatology*, vol. 137, pp. e185–e191, 2017.

[26] D. W. Piston and G.-J. Kremers, "Fluorescent protein fret: The good, the bad and the ugly," *Trends in Biochemical Sciences*, vol. 32, pp. 407–414, 2007.

[27] A. C. Miklos, C. Li, and G. J. Pielak, "Using nmr-detected backbone amide 1h exchange to assess macromolecular crowding effects on globular-protein stability," in *Methods in Enzymology*, vol. 466, pp. 1–18, Amsterdam, The Netherlands: Elsevier, 2009.

[28] N. Momenbeitollahi, T. Cloet, and H. Li, "Pushing the detection limits: Strategies towards highly sensitive optical-based protein detection," *Analytical and Bioanalytical Chemistry*, vol. 413, pp. 5995–6011, 2021.

[29] F. T. Chan, G. S. Kaminski Schierle, J. R. Kumita, C. W. Bertoncini, C. M. Dobson, and C. F. Kaminski, "Protein amyloids develop an intrinsic fluorescence signature during aggregation," *Analyst*, vol. 138, pp. 2156–2162, Apr. 2013.

[30] A. B. Biter, J. Pollet, W.-H. Chen, U. Strych, P. J. Hotez, and M. E. Bottazzi, "A method to probe protein structure from uv absorbance spectra," *Analytical Biochemistry*, vol. 587, p. 113450, 2019.

[31] A. P. Minton, "Recent applications of light scattering measurement in the biological and biopharmaceutical sciences," *Analytical Biochemistry*, vol. 501, pp. 4–22, May 2016.

[32] A. F. Charvat, K. Mason-Chalmers, and J. E. Gestwicki, "A beginner's guide to differential scanning fluorimetry," *Biochem (Lond)*, vol. 47, no. 2, pp. 11–15, 2025.

[33] C. M. Johnson, "Differential scanning calorimetry as a tool for protein folding and stability," *Archives of Biochemistry and Biophysics*, vol. 531, pp. 100–109, Mar. 2013.

[34] P. M. Ihnat, J. Zhang, J. Xu, K. Wu, and R. J. Carrillo, "High-throughput conformational and colloidal stability screening of biologic molecules," in *Development of Biopharmaceutical Drug-Device Products* (F. Jameel, J. Skoug, and R. Nesbitt, eds.), vol. 35 of *AAPS Advances in the Pharmaceutical Sciences Series*, pp. 117–138, Cham, Switzerland: Springer, 2020.

[35] M. J. Moreau, I. Morin, and P. M. Schaeffer, "Quantitative determination of protein stability and ligand binding using a green fluorescent protein reporter system," *Molecular BioSystems*, vol. 6, pp. 1285–1292, 2010.

[36] A. M. Rossi and C. W. Taylor, "Analysis of protein-ligand interactions by fluorescence polarization," *Nature Protocols*, vol. 6, pp. 365–387, 2011.

[37] T. Wu, J. Yu, Z. Gale-Day, A. Woo, A. Suresh, M. Hornsby, and J. E. Gestwicki, "Three essential resources to improve differential scanning fluorimetry (dsf) experiments," *BioRxiv*, 2020.

[38] C. Sun, Y. Li, E. A. Yates, and D. G. Fernig, "Simpledsfviewer: A tool to analyze and view differential scanning fluorimetry data for characterizing protein thermal stability and interactions," *Protein Science*, vol. 29, pp. 19–27, 2020.

[39] D. M. Jameson and S. E. Seifried, "Quantification of protein–protein interactions using fluorescence polarization," *Methods*, vol. 19, pp. 222–233, 1999.

[40] S. Pal, P. Pyne, N. Samanta, S. Ebbinghaus, and R. K. Mitra, "Thermal stability modulation of the native and chemically-unfolded state of bovine serum albumin by amino acids," *Physical Chemistry Chemical Physics*, vol. 22, pp. 179–188, 2020.

[41] K. Takeda, A. Wada, K. Yamamoto, Y. Moriyama, and K. Aoki, "Conformational change of bovine serum albumin by heat treatment," *Journal of Protein Chemistry*, vol. 8, pp. 653–659, 1989.

[42] Y. Yang, Y.-X. Ren, M. Chen, Y. Arita, and C. Rosales-Guzmán, "Optical trapping with structured light: a review," *Advanced Photonics*, vol. 3, no. 3, p. 034001, 2021.

[43] T. A. Nieminen, G. Knöner, N. R. Heckenberg, and H. Rubinsztein-Dunlop, "Physics of optical tweezers," *Methods in Cell Biology*, vol. 82, pp. 207–236, 2007.

[44] A. Ashkin, J. M. Dziedzic, and T. Yamane, "Optical trapping and manipulation of single cells using infrared laser beams," *Nature*, vol. 330, no. 6150, pp. 769–771, 1987.

[45] J. Feng, X. Shi, and et al., "Optical trapping of a single molecule of length sub-1 nm in solution," *CCS Chemistry*, vol. 5, no. 1, p. –, 2023.

[46] K. Zembrzycki, S. Pawłowska, F. Pierini, and T. A. Kowalewski, "Brownian motion in optical tweezers: A comparison between md simulations and experimental data in the ballistic regime," *Polymers*, vol. 15, no. 3, p. 787, 2023.

[47] H. A. Bethe, "Theory of diffraction by small holes," *Physical Review*, vol. 66, no. 7-8, pp. 163–182, 1944.

[48] W. L. Barnes, A. Dereux, and T. W. Ebbesen, "Surface plasmon subwavelength optics," *Nature*, vol. 424, no. 6950, pp. 824–830, 2003.

[49] Y. Pang and R. Gordon, "Nanophotonics using a subwavelength aperture in a metal film," *Nanotechnology Reviews*, vol. 1, no. 4, pp. 339–362, 2012.

[50] Y. Chen, A. Kotnala, L. Yu, J. Zhang, and R. Gordon, "Wedge and gap plasmonic resonances in double nanoholes," *Optics Express*, vol. 23, no. 23, pp. 30227–30236, 2015.

[51] M. L. Juan, R. Gordon, Y. Pang, F. Eftekhari, and R. Quidant, "Self-induced back-action optical trapping of dielectric nanoparticles," *Nature Physics*, vol. 5, no. 12, pp. 915–919, 2009.

[52] Z. Xu, W. Song, and K. B. Crozier, "Direct particle tracking observation and brownian dynamics simulations of a single nanoparticle optically trapped by a plasmonic nanoaperture," *ACS Photonics*, vol. 5, pp. 2850–2859, 2018.

[53] D. Verschueren, X. Shi, and C. Dekker, "Nano-optical tweezing of single proteins in plasmonic nanopores," *Small Methods*, vol. 3, p. 1800465, 2019.

[54] Q. Jiang, B. Rogez, J.-B. Claude, G. Baffou, and J. Wenger, "Temperature measurement in plasmonic nanoapertures used for optical trapping," *ACS Photonics*, vol. 6, pp. 1763–1773, 2019.

[55] Q. Jiang, B. Rogez, J.-B. Claude, A. Moreau, J. Lumeau, G. Baffou, and J. Wenger, "Adhesion layer influence on controlling the local temperature in plasmonic gold nanoholes," *Nanoscale*, vol. 12, pp. 2524–2531, 2020.

[56] E. H. Toodeshki, A. L. Frencken, F. C. van Veggel, and R. Gordon, "Thermometric analysis of nanoaperture-trapped erbium-containing nanocrystals," *ACS Photonics*, vol. 11, pp. 1390–1395, 2024.

[57] C. Ying, E. Karakaci, E. Bermudez-Urena, A. Ianiro, C. Foster, S. Awasthi, A. Guha, L. Bryan, J. List, S. Balog, G. P. Acuna, R. Gordon, and M. Mayer, "Watching single unmodified enzymes at work." arXiv preprint arXiv:2107.06407 [physics.bio-ph], July 2021. Available at https://arxiv.org/abs/2107.06407, accessed November 21, 2024.

[58] Y. Pang and R. Gordon, "Optical trapping of a single protein," *Nano Letters*, vol. 12, pp. 402–406, 2012.

[59] V. M. Rosenoer, M. Oratz, and M. A. Rothschild, *Albumin: Structure, Function and Uses*. Amsterdam, Netherlands: Elsevier, 2014.

[60] K. Baler *et al.*, "Electrostatic unfolding and interactions of albumin driven by ph changes: a molecular dynamics study," *J. Phys. Chem. B*, vol. 118, pp. 921–930, 2014.

[61] T. P. Jr., "Serum albumin," *Adv. Protein Chem.*, vol. 37, pp. 161–245, 1985.

[62] G. Fanali *et al.*, "Human serum albumin: from bench to bedside," *Mol. Asp. Med.*, vol. 33, pp. 209–290, 2012.

[63] D. C. Carter *et al.*, "Three-dimensional structure of human serum albumin," *Science*, vol. 244, pp. 1195–1198, 1989.

[64] M. u. d. Parray, S. Y. AlOmar, A. Alkhuriji, F. A. Wani, Z. A. Parray, and R. Patel, "Refolding of guanidinium hydrochloride denatured bovine serum albumin using pyridinium-based ionic liquids as artificial chaperons," *J. Mol. Liq.*, vol. 326, p. 115242, 2021.

[65] X. Wang and et al., "Thermal denaturation of bovine serum albumin studied by spectroscopy," *Journal of Thermal Analysis and Calorimetry*, vol. 123, pp. 1237–1245, 2016.

[66] Solutions in Plastics / ERIKS, "PETG datasheet: Vicat softening point and thermal expansion." https://solutions-in-plastics.info/nl-be/datasheets/transparante Accessed: 2024-03-02.

[67] M. Puttegowda, S. Rangappa, S. Siengchin, and M. Jawaid, "Shape-stabilized phase change materials of polyolefin/wax blends and their composites: A systematic review," *Journal of Thermal Analysis and Calorimetry*, vol. 139, no. 5, pp. 3245–3262, 2019.

[68] L. . P. T. Shenzhen Wellen Technology Co., "Tec1-12704 thermoelectric cooler module specifications," 2015.

[69] Same Sky (Formerly CUI Devices), "CP2020405H (cp20h series) thermoelectric peltier module," 2025.

[70] ProBots, "Tec1-12703 thermoelectric cooler module datasheet," 2025.

[71] J. Frenkel, "The viscosity of liquids," *Nature*, vol. 125, pp. 581–582, 1930.

[72] D. S. Viswanath and G. Natarajan, *Data Book on the Viscosity of Liquids*. New York, Washington, Philadelphia, London: Hemisphere Publishing Corporation, 1989.

[73] The Engineering ToolBox, "Thermal conductivity of common materials – solids, liquids and gases." https://www.engineeringtoolbox.com/thermal-conductivity-$d_4$29.*html*, 2003. *Accessed* : $2025 - 08 - 08$.

[74] K. Letwin, M. Peters, and R. Gordon, "Conformational stability at low temperatures using single protein nanoaperture optical tweezers," *The Journal of Physical Chemistry B*, vol. 129, no. 9, pp. 2402–2407, 2025.

[75] L. F. T. de Resende, F. C. Basilio, P. Alliprandini Filho, E. M. Therézio, R. A. Silva, O. N. Oliveira Jr, A. Marletta, and P. T. Campana, "Revisiting the conformational transition model for the ph dependence of bsa structure using photoluminescence, circular dichroism, and ellipsometric raman spectroscopy," *The Journal of Physical Chemistry B*, vol. 129, no. 9, pp. 2402–2407, 2025.

[76] H. Y. Li *et al.*, "Tier-0 protein dynamics of bovine serum albumin," *Journal of Biological Chemistry*, vol. 296, no. 3, pp. 100–110, 2020.